A fracture-based discrete model for simulating creep in quartz sands

Author 1

- Jiangtao Lei
- Division of Geotechnical Engineering and Geosciences, Department of Civil and Environmental Engineering, Polytechnic University of Catalonia (UPC), Barcelona, Spain
- 0000-0001-9458-725X

Author 2

- Marcos Arroyo
- Division of Geotechnical Engineering and Geosciences, Department of Civil and Environmental Engineering, Polytechnic University of Catalonia (UPC), Barcelona, Spain
- 0000-0001-9384-9107

Author 3

- Matteo Ciantia
- School of Science and Engineering, University of Dundee, Dundee, UK
- 0000-0003-1897-4471

Author 4

- Ningning Zhang
- Institute of Geomechanics and Underground Technology, RWTH Aachen University, Aachen, Germany
- 0000-0003-3425-8926

Full contact details of corresponding author.

Jiangtao Lei
Geotechnical Division,
Department of Civil and Environmental Engineering,
Polytechnic University of Catalonia,
D2 201, Campus Nord, Carrer de Jordi Girona, 1, 3, 08034 Barcelona,
Spain
Email: jiangtao.lei@upc.edu

Number of words in the main text: 6146
Number of Figure parts: 28
Number of Tables:3
Number of Notations:32
Number of references:74

Abstract (150 – 200 words)

Creep of granular soils is frequently accompanied by grain breakage. Stress corrosion driven grain breakage offers a micromechanically based explanation for granular creep. This study incorporates that concept into a new model based on the discrete element method (DEM) to simulate creep in sands. The model aims for conceptual simplicity, computational efficiency and ease of calibration. To this end a new form of normalized Charles power law is incorporated into a DEM model for rough-crushable sands based on the particle splitting technique. The model is implemented using a controlled on-off computational strategy. The model is validated by simulating creep in quartz sands in oedometric and triaxial conditions. Model predictions are shown to compare favourably with experimental results in terms of creep strain, creep strain rates and particle breakage. The model proposed would facilitate the calibration of phenomenological continuum models, but may be also useful to directly investigate structural scale phenomena, such as pile ageing.

Keywords chosen from ICE Publishing list

Cracks & cracking; Creep; Discrete-element modelling; Particle crushing; Time dependence;

List of notations (examples below)

δ is the particle overlap

δ_{T1}, δ_{T2} are critical contact overlaps for three transition regimes

δ_1, δ_2 are the dimentional constants

F_n is the contact normal force

F_{nT1}, F_{nT2} is the transitional contact normal forces

E_1, E_2 are young's modulus of two contacting particles

v_1, v_2 are Poisson's ratios of two contacting particles

r_1, r_2 are radii of two contacting particles

S_q is the particle roughness

A_F is the force contact area

κ_{mob}, κ are the mobilised and intrinsic strengths

χ is the microstructure parameter

ν is the Poisson's ratio

R is the particle radius

σ_{lim} is the characteristic particle limiting stress

$\sigma_{lim,0}$ is the mean particle limiting stress

d is the particle diameter

d_0 is the reference particle diameter

m_{p} is the material parameter

M_{T} is the total mass

d_{max}, d_{min} are the maximum//minimum particle diameter

β is the fractal factor

v is the crack velocity

v_0 is the reference velocity

K_c is the material toughness

n is the stress corrosion index

β_c is the crack geometry parameter

a is the crack half length

σ_t is the tensile strength

σ_{mob} is the particle maximum normal contact stress

m is the creep strain rate parameter

a_0 is the initial crack half-length

Introduction

The time-dependent behaviour of granular soils has been recognized as a crucial mechanism in many phenomena of engineering significance like the observed large shaft capacity increase with time of driven piles, known as pile set-up (Jardine *et al*., 2006; Zhang & Wang, 2015; Gavin & Igoe, 2021). From the material viewpoint, pile set-up is a particular manifestation of ageing (Schmertmann, 1991), a process by which the mechanical properties of soils improve with time without significant change in effective stress. It is currently recognized (Mitchell, 2008) that the most plausible explanation of sand ageing is given by physically-driven -as opposed to chemically or biologically mediated- micromechanical evolution. Physically-driven micromechanical evolution would necessarily involve changes in the granular contact fabric around the foundation (Bowman & Soga, 2003). However, absent any external disturbance, time changes in granular fabric can only take place if there are physical changes in the grains themselves, i.e. in their sizes, shapes or contact properties.

Laboratory studies have identified some of the physical modifications that underlie time effects in sand. It is now clear that grain crushing is associated with time dependent phenomena in sands (Colliat-Dangus *et al*., 1988; Takei *et al*., 2001; Karimpour & Lade, 2010; Brzesowsky *et al*., 2014; Lv *et al*., 2017). Direct evidence of grain fracture during experiments may be obtained with optical imaging techniques (e.g. Takei *et al*., 2001) or by means of computed tomography (Andó *et al*., 2019). More frequently, evidence for grain crushing is only obtained after the test is finished, by examining grain size distributions (GSD). This experimental procedure is not only slow and inefficient (one measurement point per sample) but also prone to error when materials are too friable or the fragments are too small (Karimpour & Lade, 2010). Physical modifications related to time effects are also present at the sub-granular scale. Asperity and roughness evolve under loading, leading to what is described as contact maturing (Michalowski *et al*., 2018). It is likely that contact maturing is more relevant at lower stress levels than grain facture. Needless to say, the experimental difficulties only increase when the physical changes to observe during specimen testing do not involve particle breakage but rather contact attrition.

Discrete-element method (DEM) based simulations are used to complement and extend difficult experimental work (e.g. Liu *et al*., 2023; Shi *et al*., 2022; Wu *et al*., 2022; Phan *et al*., 2021). DEM model results could then facilitate continuum model calibration. Also, if properly formulated, DEM models may be scaled up to directly represent problems of engineering interest (e.g. Arroyo *et al*., 2011; Ciantia *et al*., 2016a; Zhang *et al*., 2019; Cerfontaine *et al*., 2021), bypassing continuum modelling altogether. DEM may be used like a continuum phenomenological model, calibrating microscale parameters on specimen scale responses. However, DEM models are more attractive when information acquired at particle scale is leveraged to reproduce specimen-scale phenomena.

A number of studies have explored time effects in granular soils using DEM. Kuhn & Mitchell (1992, 1993), presented a 2D visco-frictional contact model, in which the tangential force acting at contacts relaxed in time with a rate that was dependent on mobilized contact friction at the same contact. The model was justified using rate process theory (RPT), by reference to atomic-scale interactions at solid contacts (silica-silica bonds), activated through thermal energy. The model achieved a strain rate decay similar to that of soils, while also recovering the influence of mobilized macroscopic strength on the onset of creep failure. The RPT model was later generalized to 3D (Kwok & Bolton, 2010), combined with a time-independent particle breakage model (Liu *et al*., 2019) or even applied to simulate rock creep (Gutierrez *et al*., 2020).

Other researchers (Wang *et al*., 2008; Wang *et al*., 2014; Tong & Wang, 2015) have used a variety of rheological models including viscous dashpots to describe contact interaction in DEM models of sand. The behaviour predicted by these models is similar to that achieved with RPT, although the contact model parameters are openly recognized as phenomenological and can only be determined by examining their effect on specimen scale response.

The physical basis claimed for RPT DEM models is frequently lost during model calibration. This is due to the difficulties inherent in using DEM to simulate long-duration experiments (creep observations in the laboratory typically last hours or days; aging in field conditions is observed for months and years). Dynamic DEM computation is advanced explicitly in time. Computational stability requirements limit the time step to values that, in most circumstances, are well below 1 μs (Otsubo *et al*., 2017b). This makes the computational load of any realistic DEM creep simulation overwhelming, if the simulated time is fully reproduced in the simulation time.

Models based on RPT have bypassed this difficulty by means of material scaling, in which some of the micromechanical model parameters are recalibrated to accelerate creep. For models based on RPT this implies scaling up the viscous parameter value (Kuhn & Mitchell, 1992; Kwok & Bolton, 2010) or, equivalently, to directly scale time (Gutierrez *et al*., 2020). The scaling factor applied is calibrated to match experimentally observed strain rate levels (Liu *et al*., 2019; Gutierrez *et al*., 2020). The resulting scaling factors are very large numbers (for instance 10^{10} in Kuhn & Mitchell) that dwarf the effect on the model viscous parameter of the physical variables (temperature, activation energy,…) that would otherwise determine its value. It is then very difficult to verify if the first-principles viscous parameter value selected is actually relevant for the material at hand.

An interesting alternative to RPT is offered by models trying to explain soil creep through sub-critical crack growth (Atkinson, 1984), as fracture propagation has an inherent time scale. This was noted by Oldecop & Alonso (2007) in connection with rockfill time-dependent deformation. DEM models of soil creep based on sub-critical crack growth have two potential advantages. One is that fracture mechanics parameters relevant to geomaterials might be measured, allowing microscale calibration. The second is that if grain breakage is included, the model output may be also verified against laboratory measurements of GSD evolution. However, these two potential advantages of fracture-based creep DEM models have not been yet fully exploited.

Kwok & Bolton (2013) showed how creep results similar to those of soils could be obtained from a DEM model based on fracture. They were using bonded agglomerates to model grains, a technique that severely curtails the number of grains that may be represented in the model and no attempt was made to compare grain size distribution outcomes with laboratory results. Fracture affected the bonds between agglomerate sub-particles and the parameters controlling bond strength degradation were calibrated on specimen-scale responses. The same model was later applied by Xu *et al*., (2018) who showed its ability to reproduce non-isotach behaviour (Tatsuoka *et al*., 2008; Lade *et al*., 2007). Calibration of bond strength degradation was done at specimen scale. Some DEM GSD curves during creep were obtained, but not compared to any laboratory result.

Charles (1958) power law was implemented into DEM to simulate the mechanical behaviour of rockfill by Tapias *et al.,* (2015) and Alonso & Tapias (2019). Grains were represented using breakable agglomerates, although fracture evolved at the agglomerate scale. The model was complex to calibrate, using a mixture of microscale and specimen scale information, like yield stress. Predictions of triaxial compression, including grain size distribution, were contrasted with experiments, with varying success. As detailed by Tapias (2016), the dynamic computational timestep was directly mapped into real time, assuming that every timestep during a creep phase represented one second in the laboratory. Since the DEM computational timestep is not independent of contact stiffness or particle size, such an approach is difficult to generalize, particularly when the simulation involves breakage or stress-induced stiffening.

Xu *et al*., (2018) used a different computational strategy: alternate or on-off computation. In this approach most of the simulated process is advanced with a simplified ageing model and the full dynamic model – run without any time or material scaling- is only switched-on when required to recover equilibrium. This on-off computational strategy had been previously applied in some DEM (Tran *et al*., 2009) or FEM-DEM models (Ma *et al*., 2015) of rockfill fracture-induced time evolution. It has also strong analogies with the high-cycle continuum models (Niemunis *et al*., 2005) applied to evaluate the effect of long-term cyclic loads.

Building on that previous work this study presents a new DEM model based on fracture to simulate creep in sands. The model conjugates conceptual simplicity, computational efficiency and ease of calibration. For the first time a DEM model for sand creep is proposed with the ability to match laboratory experiments in terms of creep strain, creep strain rates, GSD evolution and particle breakage. Thanks to the on-off computational strategy applied, the computational load is moderate even for very long real-time experiments, while still using physically based values of DEM material parameters.

2. Model description

2.1 Rough contact model

In this work we use only spherical discrete elements. A simplified Hertz-Mindlin frictional contact model (e.g. Thornton, 2015), is modified to take into account roughness effects on the normal stiffness component. The modification follows Otsubo *et al*., (2017a), who proposed a model (Figure 1) with three successive regimes to describe the influence of particle roughness on contact normal stiffness.

In this model when $\delta \le \delta_{T1}$, the contact response is in the asperity-dominated regime and:

$$F_n = F_{nT1}\left(\frac{\delta}{\delta_{T1}}\right)^c \tag{1}$$

when $\delta_{T1} < \delta < \delta_{T2}$, the contact response is in the transitional-dominated regime:

$$F_n = F_{nT2}\left(\frac{\delta-\delta_1}{\delta_{T2}-\delta_1}\right)^b \tag{2}$$

when $\delta_{T2} \le \delta$, the contact response is in the Hertzian regime:

$$F_n = \frac{4}{3}E'\sqrt{r'}(\delta-\delta_1-\delta_2)^{1.5} \tag{3}$$

where F_n is the normal contact force. E' and r' are calculated by Equation (4), (5):

$$E' = \left(\frac{1-v_1^2}{E_1}+\frac{1-v_2^2}{E_2}\right)^{-1} \tag{4}$$

$$r' = \left(\frac{1}{r_1}+\frac{1}{r_2}\right)^{-1} \tag{5}$$

In the previous equations δ is the particle overlap, E_1 and E_2 are young's modulus of the two contacting particles; v_1 and v_2 their Poisson's ratios; r_1 and r_2 their radii.

δ_{T1}, δ_{T2} are critical contact overlaps for three transition regimes that correspond to transitional contact normal forces of F_{nT1} and F_{nT2}. These are functions of roughness S_q and elastic parameters. δ_1 and δ_2 are both also functions of roughness S_q:

$$\delta_1 = n_1S_q \tag{6}$$

$$\delta_2 = n_2S_q \tag{7}$$

where n_1 and n_2 are model parameters. Parameters *b* and *c* are constants that ensure stiffness continuity, and both depend only on δ_1, δ_2, δ_{T1}, δ_{T2}. It is apparent that when $S_q = 0$, a standard Hertzian contact model is recovered. More details about the model may be found in Otsubo *et al*., (2017a).

2.2 Particle failure model

2.2.1 Time-independent failure

The time-independent particle failure model employed was introduced by Ciantia *et al.,* (2015) and has been used for several studies at the specimen scale (Ciantia *et al*., 2016b; 2019a; 2019b). The model was later refined by Zhang *et al.,* (2021) to take into account the rough contact model just introduced.

The model is inspired by analytical studies of Russell & Muir Wood (2009), who combined a two-parameter material strength criterion with the analysis of the elastic stress distribution induced by point loads on a sphere to obtain a failure criterion for the loaded particle. The limit condition was expressed as:

$$\kappa_{mob} \leq \kappa \tag{8}$$

where κ_{mob} and κ are the mobilised and intrinsic strengths of particles. Mobilized strength, in turn, is given by:

$$\kappa_{mob} = f(\chi, \nu) \frac{F_n}{\pi R^2 sin^2\theta} \tag{9}$$

where F_n is the normal force acting at a contact, *R* particle radius and θ the solid contact angle 'seen' from the centre of the sphere (Figure 2). The function $f(\chi, \nu)$ –given in Russell & Muir Wood (2009)– expresses a condition of maximum tensile stress in the sphere derived from the elastic stress distribution and strength criteria. The strength criteria (Christensen, 2004) is formulated using parameters χ and κ, but these are directly related to σ_c and σ_t the uniaxial compressive and tensile strengths of the material. Russell & Muir Wood (2009) worked out analytically that this failure criterion remains valid under multiple contact loads; Tapias *et al.,* (2015) obtained the same result using numerical simulation.

For application in DEM models, Ciantia *et al*., (2015) observed that equations (8) and (9) imply a condition on contact forces and that such condition could be expressed as the product of a material property, the characteristic particle limiting stress, σ_{lim}, and the force contact area, A_F

$$F_n \leq \frac{\kappa}{f(\chi,\nu)} \pi R^2 \sin^2\theta = \sigma_{\mathrm{lim}} A_F \quad (10)$$

This later realization led to generalize the Russell & Muir Wood (2009) failure condition. From the point of view of the material, the generalization introduced (Ciantia *et al*., 2015) was double. First, a particle size-effect was introduced in the failure criteria, and second, randomness was introduced in the strength assignment for particles of a single size, to indirectly represent the influence of aspects such as particle shape on particle breakage. This generalized particle limiting stress is implemented through an assignment of particle strength given by

$$\sigma_{\mathrm{lim}} = \sigma_{\mathrm{lim},0} \left(\frac{d}{d_0}\right)^{-\frac{1}{m_p}} (1 + X_{0,1} var) \quad (11)$$

where d is the element diameter, $\sigma_{lim,0}$ is the mean value of strength at the reference diameter d_0, and m_p a material parameter. The value *var* is the coefficient of variation of the distribution of particle strength for particles of diameter d_0, assumed normal. The symbol $X_{0,1}$ represents a random number sampled from the standard normal distribution. All the parameters relevant to the crushing model may be obtained from single particle crushing tests.

From the point of view of the force contact area, the relevant expression for the rough Hertzian contact model is

$$A_F = \pi r' \delta \quad (12)$$

With the meaning of r' and δ as given in the previous section.

Once failure takes place, a particle will split into 14 balls using a splitting scheme described in Ciantia *et al*., (2015). The sibling particles are oriented so that the local *z*-axis is aligned with the normal component of the maximum contact force (see inset in Figure 3). After that, the assignment of particle strength σ_{lim} for 14 balls will also be carried out. To ensure computational efficiency, a numerical comminution limit is imposed to stop crushing for particles smaller than a certain diameter, d_c.

The grading state index, I_G, (Muir Wood, 2007; Figure 3) is used to quantify grading evolution. It is given (Figure 3) by the area ratio of current grain size distribution (GSD) curve to a fractal limit GSD with fractal factor β =2.6:

$$\frac{M_{(L<d)}}{M_T} = \frac{d^{3-\beta} - d_{min}^{3-\beta}}{d_{max}^{3-\beta} - d_{min}^{3-\beta}} \tag{13}$$

where $M_{(L<d)}$ is the mass of particles whose diameter smaller than *d*; M_T is the total mass. d_{max} and d_{min} are maximum and minimum diameter for the sample (Table 1).

A fraction of the broken particle volume is lost upon breakage; it is assumed that the material lost corresponds to fines and those are accounted for in post-processing, to refine estimates of material grading evolution. The fractal distribution (Equation 13) is also used to estimate the GSD of the mass lost at each particle splitting event, using as d_{max} the smallest particle generated during the event. Previous studies, (Ciantia *et al*., 2015; 2016a; 2019a; 2019b; Zhang *et al*., 2021), have shown that the amount of volume lost at the specimen scale using the 14 particle split is small, and that increasing the number of siblings does not significantly modify macroscale model results.

2.2.2 Time-dependent failure

To introduce a time dependency in the failure model Charles law (1958) is used. As noted by Alonso & Tapias (2019), Charles law is simply an empirical description of experimental observations of crack growth under tensile loading, and takes the form,

$$v = v_0 (\frac{K}{K_c})^n \tag{14}$$

where v is crack velocity, v_0 is a reference velocity, K_c represents material toughness, *K* the stress intensity factor and *n* is the stress corrosion index.

Following Broek (1986), the stress intensity factor *K* for mode I (tensile) failure can be expressed as

$$K = \beta_c \sigma_I \sqrt{\pi a} \tag{15}$$

where β_c is a parameter dependent on the geometry of crack and cracked body, σ_I is the far field applied tensile stress and *a* is the crack half-length. Toughness K_c corresponds to the stress intensity at critical conditions, arrived at by increasing far field stress, crack length or both. If σ_t is the tensile strength, leading to uncontrolled crack growth for the initial fracture geometry, it results that

$$\frac{K}{K_c} = f_k \frac{\sigma_I}{\sigma_t} \tag{16}$$

where f_K is a geometry dependent term that will be characteristic of the test employed to measure toughness, of specimen size, temperature, etc. Russell & Wood (2009) note that in the Christensen material model tensile strength σ_t and limit strength κ and are proportional, so that

$$\sigma_t = \frac{\sqrt{3}}{(1+\chi)^2}\kappa = \frac{\sqrt{3}}{(1+\chi)^2} f(\chi,\nu)\sigma_{\mathrm{lim}} = f'(\chi,\nu)\sigma_{\mathrm{lim}} \tag{17}$$

They also show that the maximum elastic tensile stress along the diameter beneath a contact force is proportional to applied contact stress, so that

$$\sigma_I = f_d(\nu)\frac{F_n}{A_F} = f_d(\nu)\sigma_{\mathrm{mob}} \tag{18}$$

where σ_{mob} is the applied contact stress. It turns out that, for a point loaded sphere, with a crack aligned with the load and located at the maximum of elastic tensile stress,

$$\frac{K}{K_c} = f_k \frac{f_d(\nu)}{f'(\chi,\nu)}\frac{\sigma_{mob}}{\sigma_{\mathrm{lim}}} \tag{19}$$

This result is merely indicative for real sand grains, given the limitations of the material model, and the variability in grain shape and in the location and nature of flaws within the grain. Nevertheless, it does suggest that a reasonable time-dependent behaviour may be obtained if Charles law is applied in the DEM model simply through:

$$v = v_0\left(\frac{\sigma_{mob}}{\sigma_{\mathrm{lim}}}\right)^n \tag{20}$$

where σ_{mob} the maximum normal contact stress acting on a particle, and σ_{lim} is the particle strength; v_0 and n are the same as those in Eq. (14). Charles law is a model for crack growth, so the elements need to be seeded with initial cracks, of half-length a_0. The crack half-length a grows in time as:

$$a = a_0 + v\Delta t \tag{21}$$

where v is crack velocity, and Δt is time interval for updating the crack. To model crack propagation in the DEM model, the approach proposed by Tapias *et al.* (2016) is used. A virtual crack half-length a is treated as a particle internal variable evolving with time following eq. (21). Upon sample generation a value of a_0 uniformly distributed in the range 0.001d to 0.5d is assigned to each particle in the model. To limit the complexity of the model this approach does not aim to represent any realistic crack geometry, disregarding crack orientation and implicitly assuming a virtual crack to start from the centre of the sphere and develop radially in two diametrically opposite directions. Once the virtual crack length is equal to the particle diameter (a is equal to particle radius) the particle will fail and is replaced by the 14 particle arrangement as done for the time independent criterion. Upon breakage initial crack half-lengths a_0 are also randomly assigned to every sibling particle.

2.3 Computational strategy

In this work an off-DEM ageing technique is employed to advance the simulation during creep test phases. As shown in Figure 4 in this technique the dynamic DEM computation stages alternate with periods of off-DEM ageing. During a dynamic computation stage the discrete model runs with all its features activated: elements and boundary walls move, contacts are created or lost, contact forces and contact stresses change, assigned particle cracks grow and particles are broken if and when a breakage criterion is attained.

During off-DEM ageing periods only crack growth is active. Crack growth velocity during this phase is assumed constant, given by the mobilized contact stress determined at the end of the previous dynamic computation step. As time advances during the off-aging period the crack growth mechanism would lead to failure in some particles; such particles are identified and counted, until their number attains a certain pre-specified limit value, (n_{age}).

The dynamic DEM computation is resumed, breaking all the n_{age} particles. This creates a dynamic disruption that is computed until equilibrium is again attained until the specified creep stress state. After some sensitivity analyses (Lei *et al*., 2023) the value of n_{age} was established as 30 (0.26% of total particle number) to limit the initial disruption. The dynamic computation step is finished when stress fluctuation around the target is stabilized and a minimum number of cycles (150.000) has elapsed. All creep simulation phases start and end with a dynamic computation stage.

3. Model calibration for Fontainebleau sand

3.1 Previously calibrated Fontainebleau sand parameters

Fontainebleau sand is a quartz sand widely used in geotechnical research, which has been used as model material in previous DEM studies (Ciantia *et al*., 2015; Ciantia *et al*., 2019a; Zhang *et al*., 2021). The parameters calibrated by Zhang *et al*., (2021) for Fontainebleau sand using the rough-crushable model are reported in Table 1. It is worth noting that incorporating surface roughness enables the model to capture the initial softer response observed in experimental data (e.g. Wong & Coop, 2023) whilst using a material shear modulus *G* very similar to that of real quartz sand particles. This is different from previous DEM studies of quartz sand creep (Kwok & Bolton, 2013; Liu *et al*., 2019), where much lower *G* values were adopted to capture realistic single particle force displacement curves.

Particle rotation was inhibited to roughly simulate the interlocking effects due to non-spherical particle shapes. This is a computationally efficient simplification (Ting *et al*., 1989; Calvetti, 2008; Arroyo *et al*., 2011) that may be seen as a limit case for classical rolling-resistance contact models (Rorato *et al*., 2021).

3.2 Crack growth parameters

The two crack growth parameters to calibrate are the reference velocity v_0 and the stress corrosion index *n.* Following, Tapias *et al*. (2015; 2019) and in line with fracture growth data from by Oldecop & Alonso (2007), in this work, $v_0 = 0.1$ m/s was used. Whilst for rockfill material the presence of water is known to influence the stress corrosion index (Oldecop & Alonso, 2007), the effect of water on creep on quartz sands has been shown to be negligible (Leung *et al*., 1997; Olson *et al*., 2002). To calibrate *n*, literature data for glass, synthetic and natural quartz, and quartz rich sandstone is presented in Figure 5 and n = 60 was hence selected as a pragmatic choice for this study of quartz sands. It's worth mentioning that for rocks in general, the stress corrosion index is highly sensitive to both ambient factors (such as stress level, temperature, presence and chemistry of the pore fluid) (Brantut *et al*., 2013) and compositional factors. Both limestones and clay-rich sandstones are highly sensitive to water presence (Olson *et al*., 2002; Nara *et al*., 2012).

4. Model application

4.1 DEM model for element tests

The rough contact model and the time-independent particle failure model were implemented using the C++ plug-in capability of PFC 3D (version 5.00.40; Itasca, 2017). Time dependent failure and the off-DEM simulation advance algorithm were implemented using FISH, the high-level programming language of PFC.

Following Ciantia *et al*., (2019a), a representative cubic volumetric element (REV) of 4 mm side, containing 11500 particles, was formed using the radius expansion method. The particle size distribution (0.1 to 0.4 mm) was selected to match closely that of Fontainebleau NE34 sand. The target initial void ratio was set to 0.65 which would correspond to a relative density of 65% for the sand. Boundaries of the REV cube were set as rigid walls; wall motion was servo-controlled.

The model implementation was verified using results from a series of oedometer loading tests on Fontainebleau NE34 sand presented by Ciantia *et al*., (2019a). Figure 6 shows the results. The newly implemented DEM model agrees well with the oedometer loading curve and with the grading evolution deduced from the laboratory test series.

4.2 Creep under oedometric conditions

Brzesowsky *et al*. (2014) report results of a 2-day creep experiment on vacuum dried quartz sand (with diameter d=378$\pm 22 \mu m$) under oedometric conditions at 21.7 MPa. A creep test under the same conditions was simulated using the parameters calibrated for Fontainebleau sand. During the creep phase the constant vertical stress was enforced by continually adjusting top wall position using a stress-controlled scheme.

The simulation results are shown in Figure 7. Numbered red dots mark the episodes of dynamic computation; the time in between is off-DEM ageing time. Figure 7 shows that the simulated creep curve appears very similar to the experimental creep trend, even if no effort was made to adjust parameters to match the test results. Note that most model parameters are not specific of Fontainebleau sand. As detailed in previous work (Ciantia *et al.* 2019a; Zhang *et al.* 2021) most parameter values employed in the model were selected considering generic properties of quartz-dominated sands and other geomaterials (e.g. glass beads, sandstone). That applies to the elastic parameters (G, υ), to the parameters controlling immediate breakage (m_p, $\sigma_{lim,0}$, *var*) and to the parameters describing roughness effects on contact stiffness (S_q, n_1, n_2). Also, and perhaps most importantly, the parameters controlling fracture growth have been evaluated with reference to other quartz materials (see section 3.2). The only aspects specifically matched to Fontainebleau sand properties are the grain size distribution and the value of interparticle friction μ, selected to match a triaxial test result (see Ciantia *et al.* 2019a).

The properties of the Fontainebleau sand and the quartz sands from the Heksenberg Formation tested by (Brzesowsky et al., 2014) are presented in Table 3. As the model scales particle strength with particle size, the smaller grain size of Fontainebleau would partly explain the faster accumulation of breakage-related deformation for Heksenberg sand visible in Figure 7. It is also relevant that the void ratio before creep was slightly lower for the DEM model (at 0.584) than for the lab test (at 0.615), as looser specimens are prone to undergo more breakage (e.g. Sohn & Buscarnera, 2018).

Figure 8 shows the juxtaposed vertical stress record during the 15 dynamic computation stages that took place during the oedometer creep phase. The simultaneous breakage enforced to start every dynamic computation stage creates a small shock that is rapidly damped by the boundary stress-control algorithm. It can be seen that the amplitude of the vertical stress fluctuation remains below 4% of the target creep stress. Although the number of particles to break at the beginning of every dynamic computation remains constant, the response recorded at the different dynamic computation stages presents some variation.

4.3 Creep under triaxial conditions

To simulate creep under triaxial conditions the REV was first loaded isotropically up to a confining stress of 10 MPa. From the oedometer test results (Figure 7) this stress level was expected to guarantee significant particle breakage during shearing. A strain-controlled standard triaxial compression path was then applied with top wall velocity slow enough (0.01 m/s) to avoid any inertial effects, (resulting inertial number $I < 2.68\times10^{-4}$).

The test was initially taken to failure (at 30% deviatoric strain) to identify the available shear strength. This corresponded to a maximum deviatoric stress q_{max} of 22.6 MPa. Ten creep tests were then performed with deviatoric stress maintained constant at different fractions of the maximum (q/q_{max} values between 0.2, and 0.9). In those tests the specimen was first loaded to the desired level of mobilized strength and then deviatoric stress was maintained for at least 10^4 s, unless shear failure was attained before.

Some examples of the deviatoric stress evolution plots obtained in the triaxial tests are illustrated in Figure 9. As in the oedometer, there are some dynamic oscillations around the deviatoric creep stress, but they remain limited, smaller, for instance, than the oscillations due to continuous shear at failure during the monotonic reference path.

Figure 10 shows the volumetric strain versus axial strain plots for the creep phase. Shearing creep strains are accompanied always by volumetric contraction. This contractive creep was also observed by Karimpour & Lade (2013) when testing Virginia Beach sand at high confining pressures (8 MPa). Creep strains are more contractive at lower deviatoric stress levels than at higher ones, as observed by Lv *et al.* (2017) in their laboratory tests of quartz and coral sands.

Figure 11 shows axial strain ε_a evolution during the simulated creep phases. Creep strain is linear on log time when mobilized strength q/q_{max} lies below a certain limit (0.7 in this study). When q/q_{max} exceeds this value, obvious inflection points can be observed, and creep strain accumulates at faster rates leading to creep failure. This is classically described as tertiary creep (Augustensen *et al*., 2004) and has been observed in similar triaxial experiments on quartz sands both at high confining stress (Karimpour & Lade, 2013; $q/q_{max} > 0.8$) and at low confining stress (Murayama *et al*., 1985; $q/q_{max} > 0.95$).

Before the onset of creep failure the axial strain rate $\dot{\varepsilon}$ decreases in time. As shown in Figure 12(a) an approximate linear evolution can be observed when plotting the creep strain data in a double log axis diagram. This is characteristic of primary creep. When creep takes place at higher mobilized strength the strain rate remains briefly constant (secondary creep) and then increases (tertiary creep). That sequence, however, is not always monotonous and some oscillations between increasing and decreasing strain rates are visible in tests creeping close to shear failure (q/q_{max} above 0.8). Similar oscillations were also present in laboratory triaxial creep tests at high mobilised shear strength in friable Antelope Valley sand (Lade & Liu, 1998).

DEM simulation results at q/q_{max}= 0.4 and q/q_{max}= 0.75 were selected to compare with triaxial creep results of Virgina beach sand at the same mobilized ratios (Karimpour & Lade, 2010; 2013). The comparisons (Figure 12b) show good agreement with the experimental results during primary creep. In the case of q/q_{max}= 0.75, the strain rate tends to stabilize in both cases at the end of creep although the tertiary creep phase appears earlier in the Fontainebleau DEM experiments.

It is customary to describe the strain rate evolution during creep using the *m* parameter defined by Singh and Mitchell (1968) as:

$$m = -\frac{\Delta log\dot{\varepsilon}}{\Delta log t} \tag{22}$$

Linear regression was applied to obtain *m* values from the test data. Some example fits are illustrated in (Figure 13). Following Augustesen *et al*. (2004), the fit is only applied to the primary creep section. To compare with the existing experimental results, the strain rate (%/min) at 10 min ($\dot{\varepsilon}_{10min}$) was also obtained. All the strain rate parameters are presented in Table 2.

The strain rate *m* parameter obtained from the DEM simulations is presented in Figure 14(a) alongside previous laboratory and DEM simulation results. The *m* value obtained here is practically independent of deviatoric creep stress (Figure 14a) as observed on the laboratory tests of Toyoura quartz sand (Murayama *et al*., 1984) and tailings sand (Mejia *et al*., 1988).

This independence of *m* on stress level is also presented on the RPT-based 2D DEM simulations of Kuhn & Mitchell (1993), who excluded creep rupture data from their fit. A similar trend is visible –with less clarity- on the RPT-based 3D DEM simulation of Kwok & Bolton (2010). By way of contrast the bond strength degradation model of Kwok & Bolton (2013) shows a strong reduction of *m* as the mobilized strength at creep was increased. This comparison might be affected by the criteria -not always explicit- employed by different authors to fit the *m* parameter.

A simpler comparison may be established in terms of creep strain rate magnitude. Figure 14(b) shows its value evaluated 10 min after the initiation of creep. The results from this work fit nicely within the range of the experimental data, with the more friable tailing materials showing faster rates, the low-stress tests on quartz Toyoura showing slower creep rates and the high stress tests on quartz Virginia beach sand closer to the simulations. Interestingly, by this measure the RPT based simulations are those further off the experiments, whereas the bond-strength based Kwok & Bolton (2013) model lies closer to the results presented in this study.

4.4 Grading evolution during triaxial creep

GSD curves during triaxial creep were obtained during the simulations. Figure 15 illustrates the results for q/q_{max}=0.2, 0.5, 0.7, and 0.9. As mobilized strength at creep increases the shift of the PSD curves is more significant.

The breakage-driven nature of the creep strains is also made transparent when the evolution of the grading index with time is represented, as done in Figure 16. The similitudes with Figure 11 are notable, for instance in the inflection points noted at values of q/q_{max} above or equal to 0.75.

The amount of breakage during creep is expressed through the change in breakage index in Figure 17. The results from the simulation are very similar to those measured after laboratory experiments on Virginia beach sand by Karimpour & Lade (2013), although breakage accumulation is somewhat faster in Virginia sand. As it was the case for the previous comparison with Heksenberg sand, this discrepancy may be partly explained by the smaller grain size of Fontainebleau (Table 3).

Note that, for the purpose of this comparison, four creep simulations were extended to last one day, to match the creep period in the original lab experiments. Most of that period was simulated as off-DEM ageing, whereas the time simulated using dynamic DEM computation (less than 0.1s) was only a minimal fraction of that period. The computer running time (using a workstation with an CPU of 12th Gen Intel(R) Core(TM) i9-12900K (3.20 GHz) and 32GB RAM) extended to 41h for the most demanding case (that with q/q_{max} of 0.85). The vast majority (>99,9%) of running time was spent on the dynamic DEM computations. The practical advantages of the computational strategy adopted are thus evident.

5. Discussion

The DEM model presented is highly idealized, in that some fundamental sand grain features such as shape are only indirectly accounted for through particle strength variability, rotation blocking, etc. Also, the link between roughness and contact friction has not been considered, nor the possibility of inducing a low stress time-dependent mechanism through evolving roughness. Despite those limitations it is likely that the model micromechanics might be usefully exploited to gain insight into macroscopic features. As an example, Figure 18 presents the evolution of the broken fraction of particles of certain size ranges, d_i. This fraction is obtained as the cumulative number of particles of size d_i broken to time t divided by the current number of particles of size d_i at time t. The graph indicates not just that larger particles break more –something that follows from particle strength size dependency- but that tertiary creep is characterized by an increased participation of larger particles on breakage, as the broken fraction increases faster with particle size.

Laboratory compression experiments on relatively uniform and large glass beads (Takei *et al*., 2001) showed jumps on creep strain associated with breakage events. In continuously graded specimens DEM studies with unbreakable particles (e.g. Liu *et al*., 2023) have shown that strong force chains are preferentially channelled through larger particles. The non-monotonous increase in strain rates observed during tertiary creep in Figure 11 may be thus related to the faster breakage rate of the larger particles.

Another peculiarity of the model presented is that time-dependent breakage parameters were calibrated using fracture data from larger quartz-dominated specimens. This was done for pragmatic reasons, to avoid the experimental and statistical complexity of trying to measure fracture growth on isolated sand grains. It is thus interesting to consider the results in Figure 19, showing the effect of normalized creep stress on the time elapsed until the onset of the tertiary creep phase (known as time to failure) in the simulations and in sandstone creep experiments. Note that in the sandstone data creep and failure stress levels are net of the post-fracture residual frictional stress (Brantut *et al*., 2013). That is the stress level at which all cohesion is lost and shear strength is purely frictional, which, by analogy, is taken as zero for sands. The comparison is favourable and supports the relevance of sandstone subcritical crack growth measurements for the understanding of sand creep.

6. Conclusion

This work has described a discrete element model to explain time effects in sands based on subcritical crack growth. The model has been applied to study creep at large stress in quartz sand and the results obtained compare favourably with available experimental evidence in terms of creep strain, creep strain rates and grading evolution. Previous DEM models of sand creep had not resulted in such a wide agreement with independent laboratory experimental work. The continuous IG evolution during creep can be captured using this model, something which is almost impossible to do in laboratory tests. An increased participation of larger particles on breakage during tertiary creep was first made transparent, and this is significant to understand sand creep behaviour. The model has been implemented using a simple but efficient on-off computational strategy to get rid of the overwhelming computational load associated with long creep tests in DEM. Importantly, this computational strategy does not interfere with material parameter determination.

The model may be applied as it is to study some of the fundamental controls on sand creep, such as relative density (Colliat-Dangus *et al*., 1983) or initial grading (Karimpour & Lade, 2013) as well as other time-related phenomena like stress relaxation and, including a suitable time-scaling procedure, to examine the effect of variable strain rate. It is also easy to envisage some relevant model generalizations: for instance, as it is based on a contact law that features grain roughness, it may be also simply adapted to represent low-stress time-dependent contact maturing. The use of models such as this will likely facilitate the study of time dependent phenomena in granular materials.

Acknowledgements

The first author is supported by a Chinese Government Scholarship (CSC No.202108390006). Spanish Research Agency support (AEI) through research project PID2020-119598RB-I00 is also acknowledged.

References

Alonso, E. E. & Tapias, M. A. (2019). Suction and time effects in rockfill deformation. *International Journal for Numerical and Analytical Methods in Geomechanics* 43(5): 1032–1050. https://doi.org/10.1002/nag.2916

Andò, E., Dijkstra, J., Roubin, E., Dano, C. & Boller, E. (2019). A peek into the origin of creep in sand. *Granular matter* 21(1): 1-8.

Arroyo, M., Butlanska, J., Gens, A., Calvetti, F. & Jamiolkowski, M. (2011). Cone penetration tests in a virtual calibration chamber. *Géotechnique* 61(6): 525–531. https://doi.org/10.1680/geot.9.P.067

Atkinson, B. K. (1984). Subcritical crack growth in geological materials. *Journal of Geophysical Research* 89(B6): 4077–4114.

Augustesen, A., M. Liingaard, and P. V. Lade. (2004). Evaluation of time dependent behavior of soils. *International Journal of Geomechanics* 4(3): 137–156. https://doi.org/10.1061/(ASCE)1532-3641(2004)4:3(137)

Bowman, E. T., and K. Soga. (2003). Creep, ageing and microstructural change in dense granular materials. *Soils and Foundations* 43(4): 107–117. https://doi.org/10.3208/sandf.43.4_107

Brantut, N., Heap, M. J., Meredith, P. G., & Baud, P. (2013). Time-dependent cracking and brittle creep in crustal rocks: A review. *Journal of Structural Geology* 52: 17-43.

Broek, D. (1986). *Elementary engineering fracture mechanics*. Dordrecht: Martinus Nijhoff.

Bruner, W.M. (1980). Effects of time-dependent crack growth on the unroofing and unloading behaviour of rock. PhD. thesis. *University of California*, Los Angeles (USA).

Brzesowsky, R. H., Hangx, S. J. T., Brantut, N., & Spiers, C. J. (2014). Compaction creep of sands due to time-dependent grain failure: Effects of chemical environment, applied stress, and grain size. *Journal of Geophysical Research: Solid Earth* 119(10): 7521–7541. https://doi.org/10.1002/2014JB011277

Calvetti, F. (2008). Discrete modelling of granular materials and geotechnical problems. *European Journal of Environmental and Civil Engineering* 12(7–8): 951–965.

Cerfontaine, B., Ciantia, M., Brown, M. J., & Sharif, Y. U. (2021). DEM study of particle scale and penetration rate on the installation mechanisms of screw piles in sand. *Computers and Geotechnics* 139: 104380.

Charles, R. J. (1958). Static fatigue of glass. *Journal of Applied Physics* 29(11): 1549–1560.

Christensen, R. M. (2000). Yield functions, damage states, and intrinsic strength. *Mathematics and Mechanics of Solids* 5(3): 285–300

Ciantia, M. O., Arroyo, M., Calvetti, F., & Gens, A. (2015). An approach to enhance efficiency of dem modelling of soils with crushable grains. *Géotechnique* 65(2): 91–110. https://doi.org/10.1680/geot.13.P.218

Ciantia, M. O., Arroyo, M., Butlanska, J., & Gens, A. (2016a). DEM modelling of cone penetration tests in a double-porosity crushable granular material. *Computers and Geotechnics* 73: 109-127.

Ciantia, M. O., Arroyo, M., Calvetti, F., & Gens, A. (2016b). A numerical investigation of the incremental behavior of crushable granular soils. *International Journal for Numerical and Analytical Methods in Geomechanics* 40(13): 1773-1798.

Ciantia, M. O., Arroyo, M., O'Sullivan, C., Gens, A., & Liu, T. (2019a). Grading evolution and critical state in a discrete numerical model of Fontainebleau sand. *Géotechnique* 69(1): 1–15. https://doi.org/10.1680/jgeot.17.P.023

Ciantia, M. O., Arroyo, M., O'Sullivan, C., & Gens, A. (2019b). Micromechanical inspection of incremental behaviour of crushable soils. *Acta Geotechnica* 14(5): 1337-1356.

Colliat-Dangus, J. L., Desrues, J., & Foray, P. (1988). Triaxial testing of granular soil under elevated cell pressure. In *ASTM International. Advances triaxial testing of soil and rock*, pp. 290-310.

Enomoto, T., Koseki, J., Tatsuoka, F., & Sato, T. (2016). Creep failure of natural gravelly soil and its simulation. *Géotechnique* 66(11): 865–877. https://doi.org/10.1680/jgeot.15.P.144

Gavin, K., & Igoe, D. (2021). A field investigation into the mechanisms of pile ageing in sand. *Géotechnique* 71(2): 120–131. https://doi.org/10.1680/jgeot.18.P.235

Gutiérrez-Ch, J.G., Senent, S., Estebanez, E., Jimenez, R., 2020. Discrete element modelling of rock creep behaviour using rate process theory. *Canadian Geotechnical Journal* 58(8): 1231–1246. https://doi.org/10.1139/cgj-2020-0124

Heap, M.J., Baud, P., Meredith, P.G et al. 2011. Brittle creep in basalt and its application to time-dependent volcano deformation. *Earth and Planetary Science Letters* 307(1-2): 71-82

Holder, J., Olson, J.E., & Philip, Z. Experimental determination of subcritical crack growth parameters in sedimentary rock. *Geophysical Research Letters* 28(4):599-602.

Itasca, 2017. PFC – particle flow code, ver. 5.0. Minneapolis, MN, USA: Itasca Consulting Group.

Jardine, R. J., Standing, J. R., & Chow, F. C. (2006). Some observations of the effects of time on the capacity of piles driven in sand. *Géotechnique*, *56*(4): 227–244. https://doi.org/10.1680/geot.2006.56.4.227

Karimpour, H., & Lade, P. v. (2010). Time Effects Relate to Crushing in Sand. *Journal of Geotechnical and Geoenvironmental Engineering* *136*(9): 1209–1219. https://doi.org/10.1061/(asce)gt.1943-5606.0000335

Karimpour, H., & Lade, P.V. (2013). Creep behavior in Virginia Beach sand. *Canadian Geotechnical Journal* 50(11): 1159–1178. https://doi.org/10.1139/cgj-2012-0467

Kuhn, M. R. & Mitchell, J. K. (1993). New perspectives on soil creep. *ASCE Journal of Geotechnical Engineering* 119(3): 507–524.

Kuhn, M. R., & Mitchell, J. K. (1992). Modelling of soil creep with the discrete element method. *Engineering computations* 9(2):277-287. https://doi.org/10.1108/eb023866

Kwok, C. Y., & Bolton, M. D. (2010). DEM simulations of thermally activated creep in soils. *Géotechnique*, 60(6): 425–433. https://doi.org/10.1680/geot.2010.60.6.425

Kwok, C. Y., & Bolton, M. D. (2013). DEM simulations of soil creep due to particle crushing., *Géotechnique* 63(16): 1365–1376. https://doi.org/10.1680/geot.11.P.089

Lade, P. V., and C.-T. Liu. (1998). Experimental study of drained creep behavior of sand. *Journal of Engineering Mechanics* 124(8): 912–920. https://doi.org/10.1061/(ASCE)0733-9399(1998)124:8(912).

Lade, P. V. (2007). Experimental study and analysis of creep and stress relaxation in granular materials. In *Advances in Measurement and Modeling of Soil Behavior* pp. 1-11.

Lei, J., Arroyo, M., Ciantia, M. & Zhang, N. (2023) A time-to-fracture DEM model for simulating creep in rough crushable sand, submitted to NUMGE 2023, *10th European Conference on Numerical Methods in Geotechnical Engineering, London, UK.*

Leung, C. F., Lee, F. H., & Yet, N. S. (1997). The role of particle breakage in pile creep in sand. Canadian Geotechnical Journal 33(6): 888-898

Liu, D., O'Sullivan, C., & Carraro, J. A. H. (2023). The influence of particle size distribution on the stress distribution in granular materials. Géotechnique 73(3): 250-264.

Liu, S., Wang, J., & Kwok, C. Y. (2019). DEM Simulation of Creep in One-Dimensional Compression of Crushable Sand. *Journal of Geotechnical and Geoenvironmental Engineering* 145(10). https://doi.org/10.1061/(asce)gt.1943-5606.0002098

Lv, Y., Li, F., Liu, Y., Fan, P., & Wang, M. (2017). Comparative study of coral sand and silica sand in creep under general stress states. *Canadian Geotechnical Journal*, 54(11): 1601-1611.

Ma, G., Zhou, W., Ng, T. T., Cheng, Y. G., & Chang, X. L. (2015). Microscopic modeling of the creep behavior of rockfills with a delayed particle breakage model. *Acta Geotechnica*, 10(4): 481-496.

Mejia, C. A., Vaid, Y. P. & Negussy, D. (1988). Time dependent behaviour of sand. In *International conference on rheology and soil mechanics* (ed. M. J. Keedwell), Elsevier, London, UK, pp.312–326.

Michalowski, R. L., Wang, Z., & Nadukuru, S. S. (2018). Maturing of contacts and ageing of silica sand. *Géotechnique* 68(2): 133-145

Mitchell, J. K. (2008). Aging of sand–a continuing enigma? *Proceedings of the 6th international conference on case histories in geotechnical engineering*, Missouri University of Science and Technology (2008), USA.

Muir Wood, D. (2007). The magic of sands—the 20th Bjerrum Lecture presented in Oslo, 25 November 2005. *Canadian Geotechnical Journal*, 44(11): 1329-1350.

Murayama, S., Michihiro, K. & Sakagami, T. (1984). Creep characteristics of sands. *Soils and Foundations* 24(2): 1–15.

Nara, Y., Morimoto, K., Hiroyoshi, N., Yoneda, T., Kaneko, K., & Benson, P. M. (2012). Influence of relative humidity on fracture toughness of rock: implications for subcritical crack growth. *International Journal of Solids and Structures* 49(18): 2471-2481.

Niemunis, A., Wichtmann, T., & Triantafyllidis, T. (2005). A high-cycle accumulation model for sand. *Computers and geotechnics* 32(4): 245-263.

Oldecop, L. & Alonso, E. (2007). Theoretical investigation of the time-dependent behaviour of rockfill. *Géotechnique 57*(3): 289–301, http://dx.doi.org/10.1680/geot.2007.57.3.289.

Olson, J. E., Holder, J., & Rijken, P. (2002). Quantifying the fracture mechanics properties of rock for fractured reservoir characterization. In *SPE/ISRM Rock Mechanics Conference*. OnePetro.

Otsubo, M., O'Sullivan, C., Hanley, K. J., & Sim, W. W. (2017a). The influence of particle surface roughness on elastic stiffness and dynamic response. *Géotechnique* 67(5): 452–459. https://doi.org/10.1680/jgeot.16.P.050

Otsubo, M., O'Sullivan, C., & Shire, T. (2017b). Empirical assessment of the critical time increment in explicit particulate discrete element method simulations. *Computers and Geotechnics* 86: 67-79.

Phan, Q. T., Bui, H. H., Nguyen, G. D., & Bouazza, A. (2021). Effect of particle rolling resistance on drained and undrained behaviour of silty sand. *Acta Geotechnica*16: 2657-2682.

Rorato, R., Arroyo, M., Gens, A., Andò, E., & Viggiani, G. (2021). Image-based calibration of rolling resistance in discrete element models of sand. *Computers and Geotechnics* 131: 103929.

Russell, A. R., & Muir Wood, D. (2009). Point load tests and strength measurements for brittle spheres. *International Journal of Rock Mechanics and Mining Sciences* 46(2): 272–280. https://doi.org/10.1016/j.ijrmms.2008.04.004

Schmertmann. (1991). The mechanical aging of soils. ASCE *Journal of Geotechnical Engineering* 117(9):1288-1330.

Shi, K., Zhu, F., & Zhao, J. (2022). Multi-scale analysis of shear behaviour of crushable granular sand under general stress conditions. *Géotechnique* 1-18. https://doi.org/10.1680/jgeot.21.00412

Singh, A., Mitchell, J. K. (1968). General stress–strain–time function for soils. *Journal of the Soil Mechanics and Foundations Division* 94(1).

Sohn, C., Buscarnera, G. (2019). Measurement and simulation of comminution rate in granular materials subjected to creep tests. Granular Matter, 21(3).

Takei, M., O. Kusakabe, and T. Hayashi. (2001). Time-dependent behavior of crushable materials in one-dimensional compression tests. *Soils and Foundations* 41(1): 97–121. https://doi.org/10.3208/sandf.41.97.

Tatsuoka, F., Di Benedetto, H., Enomoto, T., Kawabe, S., & Kongkitkul, W. (2008). Various viscosity types of geomaterials in shear and their mathematical expression. *Soils and Foundations* 48(1), 41-60.

Tapias, M. (2016). Particle model for crushable aggregates which includes size, time and relative humidity effects. PhD Thesis, *Universitat Politecnica de Catalunya*, Barcelona. https://upcommons.upc.edu/handle/2117/106495

Tapias, M., Alonso, E. E., & Gili, J. (2015). A particle model for rockfill behaviour. *Géotechnique* 65(11): 975–994. https://doi.org/10.1680/geot.14.P.170

Thornton, C. *Granular Dynamics, Contact Mechanics and Particle System Simulations: A DEM Study*; Springer: Birmingham, UK, 2015; Volume 24

Ting, J. M., Corkum, B. T., Kauffman, C. R. & Greco, C. (1989). Discrete numerical model for soil mechanics. ASCE *Journal of Geotechnical Engineering* 115(3): 379–398

Tong, L., & Wang, Y. H. (2015). DEM simulations of shear modulus and damping ratio of sand with emphasis on the effects of particle number, particle shape, and aging. *Acta Geotechnica* 10(1): 117–130. https://doi.org/10.1007/s11440-014-0331-2

Tran, T. H., Vénier, R., & Cambou, B. (2009). Discrete modelling of rock-ageing in rockfill dams. *Computers and Geotechnics* 36(1-2): 264-275

Wang, Y. H., Lau, Y. M., & Gao, Y. (2014). Examining the mechanisms of sand creep using DEM simulations. *Granular Matter* 16(5): 733–750. https://doi.org/10.1007/s10035-014-0514-4

Wang, Y.-H., Xu, D., & Tsui, K. Y. (2008). Discrete Element Modeling of Contact Creep and Aging in Sand. *Journal of Geotechnical and Geoenvironmental Engineering* 134(9):1407-1411. https://ascelibrary.org/doi/full/10.1061/(ASCE)1090-0241(2008)134:9(1407)

Wong, C. P., & Coop, M. R. (2023). The contact mechanics of a UK railway ballast. *Géotechnique*, 1-13. https://doi.org/10.1680/jgeot.22.00190

Wu, M., Wang, J., & Zhao, B. (2022). DEM modeling of one-dimensional compression of sands incorporating statistical particle fragmentation scheme. Canadian Geotechnical Journal 59(1): 144-157.

Xu, M., Hong, J., & Song, E. (2018). DEM study on the macro-and micro-responses of granular materials subjected to creep and stress relaxation. *Computers and Geotechnics* 102: 111-124.

Zhang, N., Ciantia, M. O., Arroyo, M., & Gens, A. (2021). A contact model for rough crushable sand. *Soils and Foundations* 61(3): 798–814. https://doi.org/10.1016/j.sandf.2021.03.002

Zhang, N., Arroyo, M., Ciantia, M. O., Gens, A., & Butlanska, J. (2019). Standard penetration testing in a virtual calibration chamber. *Computers and Geotechnics* 111: 277-289.

Zhang, Z., & Wang, Y. H. (2015). Examining Setup Mechanisms of Driven Piles in Sand Using Laboratory Model Pile Tests. *Journal of Geotechnical and Geoenvironmental Engineering* 141(3). https://doi.org/10.1061/(ASCE)gt.1943-5606.0001252

Tables

Table 1 Calibration parameters for time-to-fracture rough-crushable model

particle failure criterion									Contact roughness			Crack propagation	
G/GPa	ν	μ	m_p	$\sigma_{lim,0}$/GPa	var	d_c/d_{50}	d_{max}/mm	d_{min}/mm	$S_q/\mu m$	n_1	n_2	v_0	n
32	0.19	0.275	12	3.75	0.38	0.55	0.27	0.01	0.6	0.05	5	0.1	60

Table 2. Triaxial creep strain rate parameters

q/q_{max}	0.2	0.3	0.4	0.5	0.6	0.7	0.75	0.8	0.85	0.9
m	0.7713	0.7356	0.7903	0.7484	0.7353	0.7246	0.7360	0.7238	0.723	0.7251
$\dot{\varepsilon}_{10min}$ (%/min)	0.00043	0.001	0.0017	0.0038	0.0086	0.0263	0.0558	0.1247	0.30	0.855

Table 3. Basic properties of different quartz sands considered in this study

Property	Units	Virginia beach sand (Karimpour & Lade 2013)	Heksenberg Formation sand (Brzesowsky et al., 2014)	Fontainebleau sand NE 34 (Ciantia et al. 2019a)
Median grain size, d_{50}	mm	0.638	0.378	0.21
Uniformity coefficient		1.4	1.12	1.53
Min. void ratio, e_{min}		0.53	Unknown	0.51
Max. void ratio, e_{max}		0.759	Unknown	0.9
Specific gravity, ρ_s		2.65	2.65	2.65
Shape descriptor		subangular	subrounded	subangular

Figures

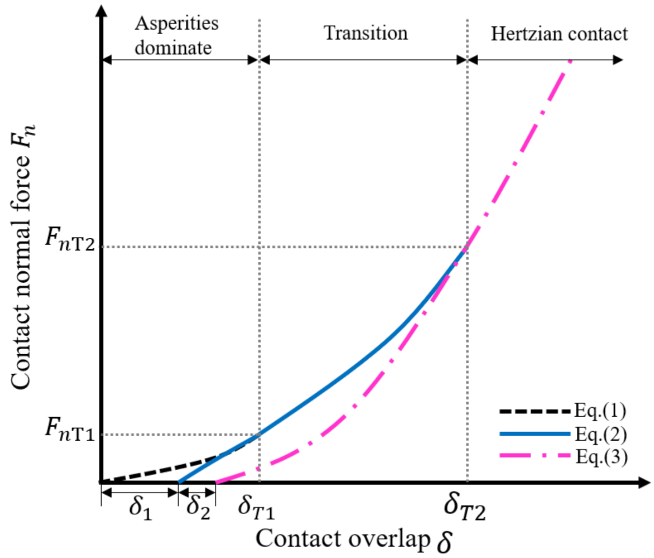

Figure 1. Rough surface normal contact model (adapted from Otsubo *et al*., 2017a)

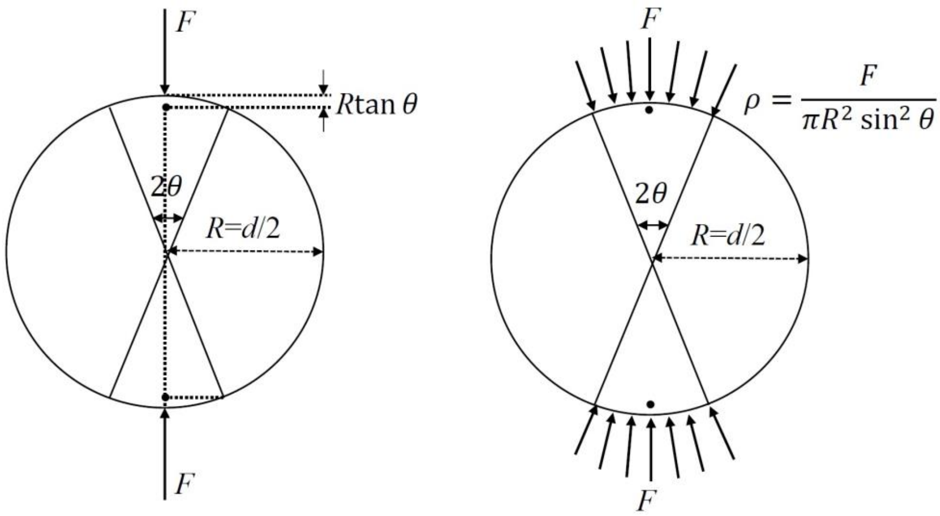

Figure 2. Contact geometry description in the failure model

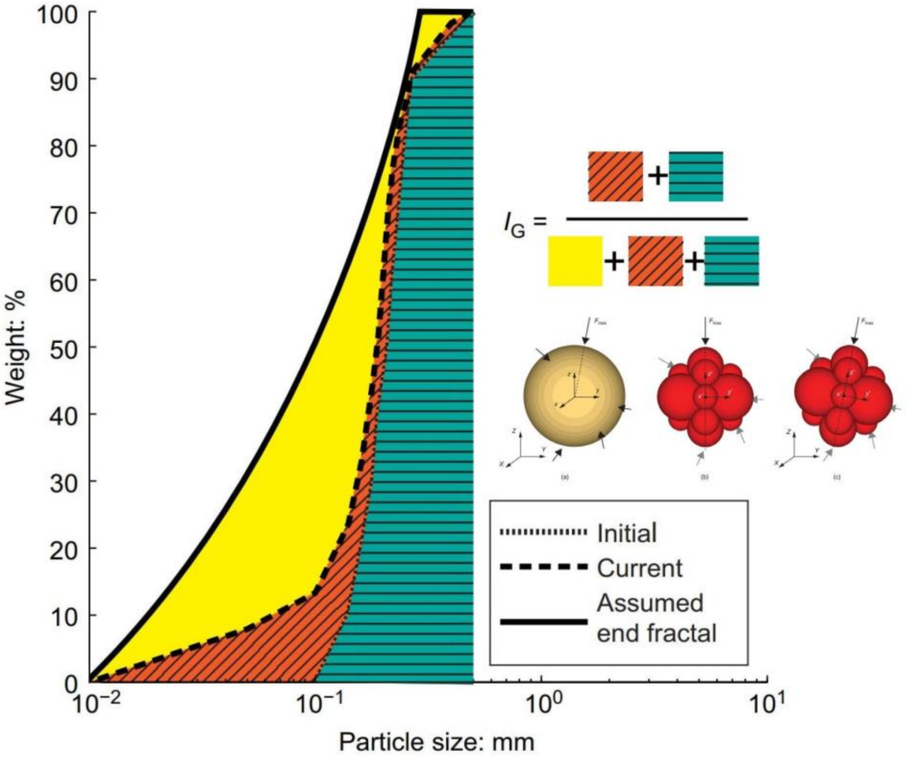

Figure 3. Schematic definition of grading index I_G and (inset) particle split model

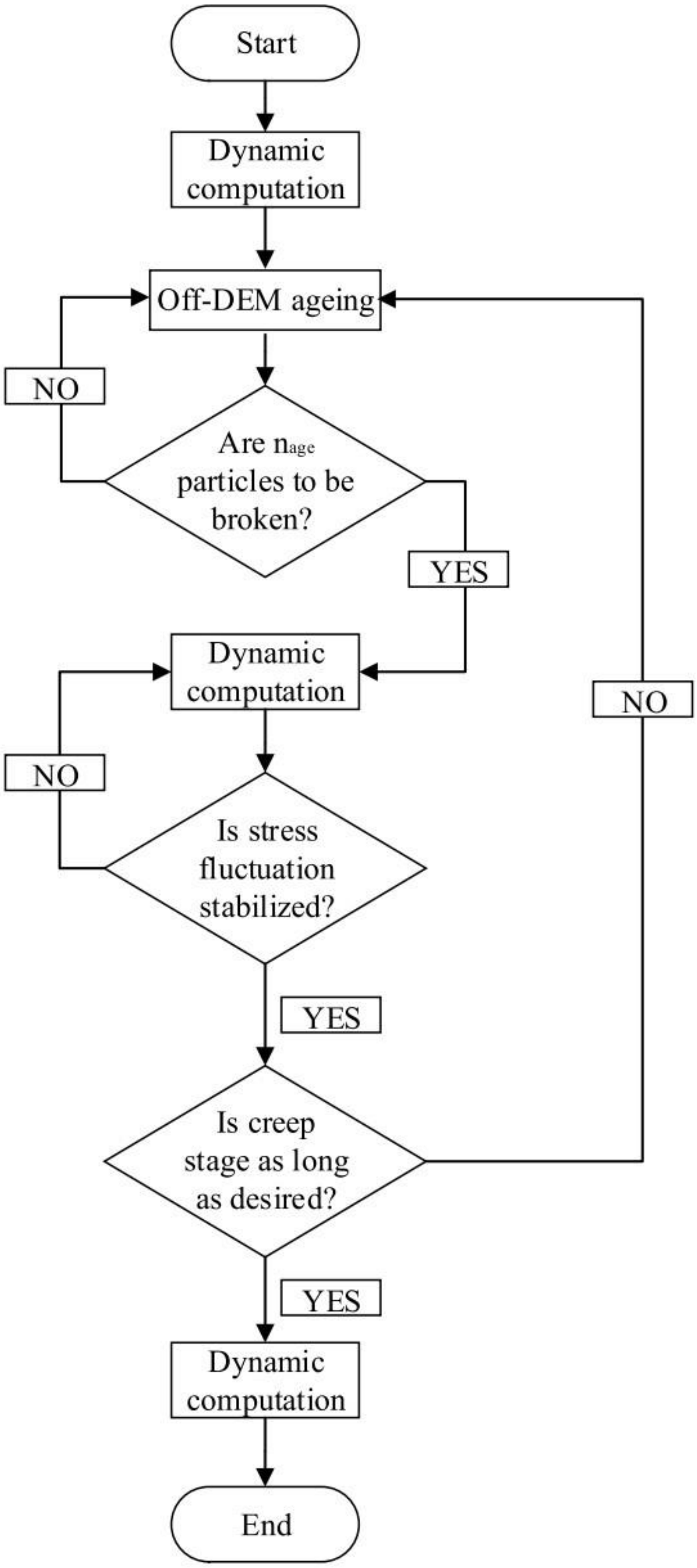

Figure 4. Flow chart for on-off DEM computation during creep phases

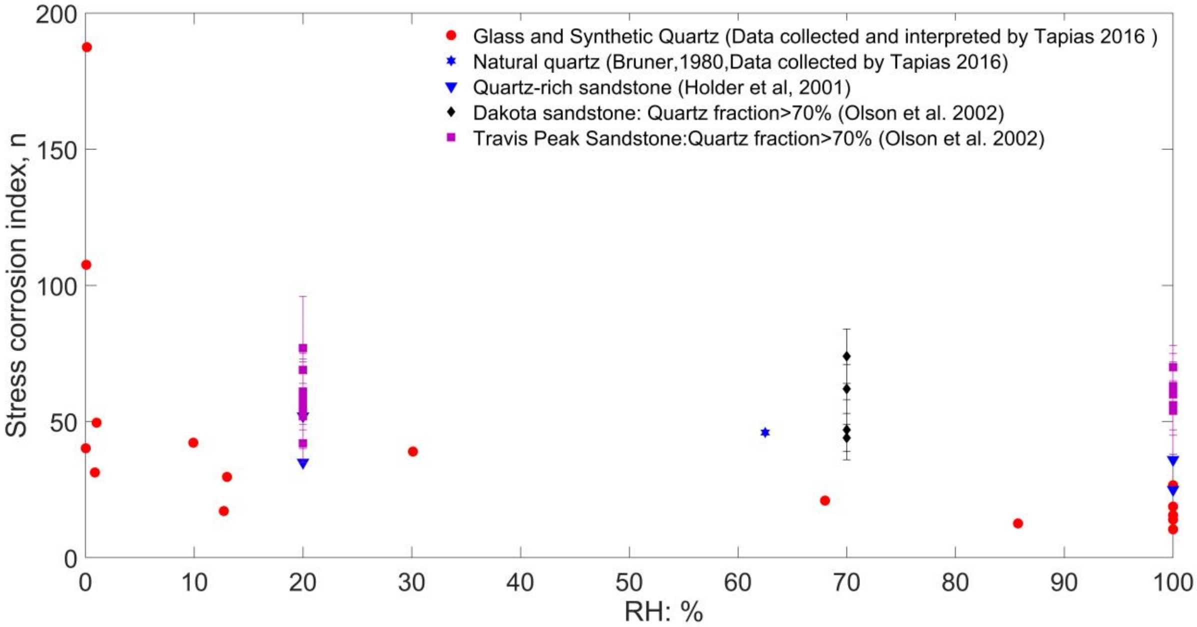

Figure 5. Stress corrosion index data for some materials relevant to quartz sands

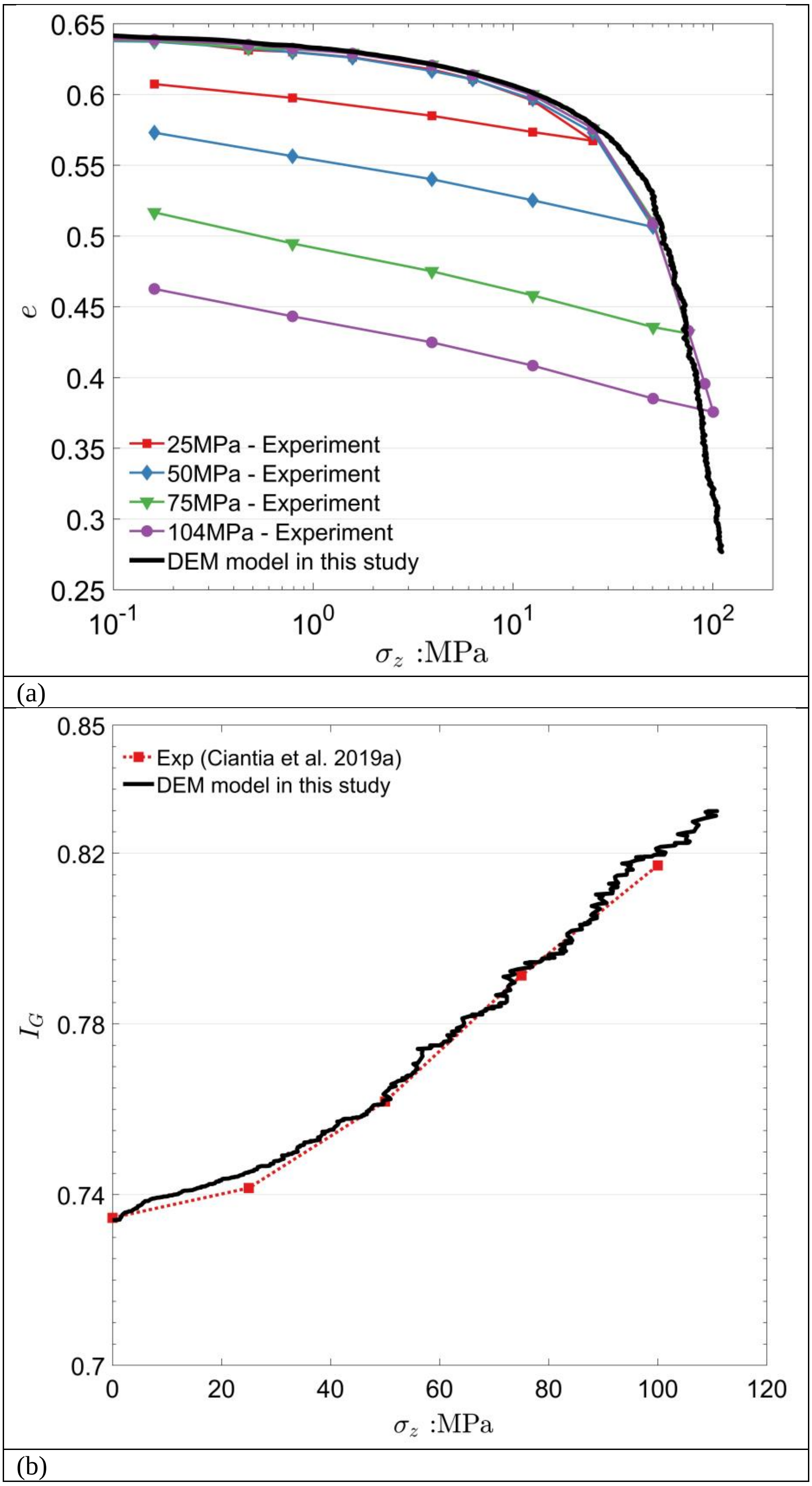

Figure 6. Oedometer test calibration against experiments reported by Ciantia *et al*. (2019a): (a) void ratio e vs vertical stress σ_z (b) I_G evolution with σ_z

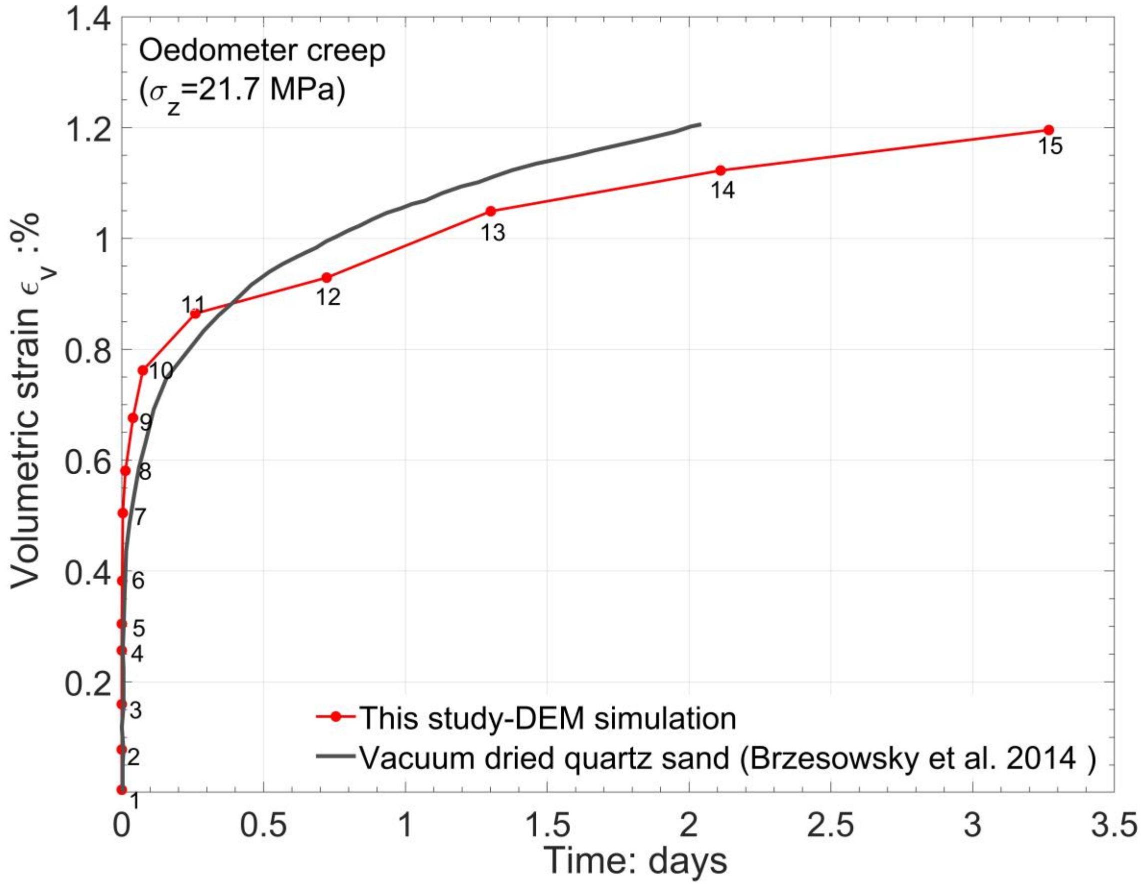

Figure 7. Oedometric creep: simulation for the calibrated Fontainebleau sand and experimental result for vacuum dried quartz sand (Brzesowsky *et al*., 2014). Dots in the simulation curve correspond to dynamic computation stages.

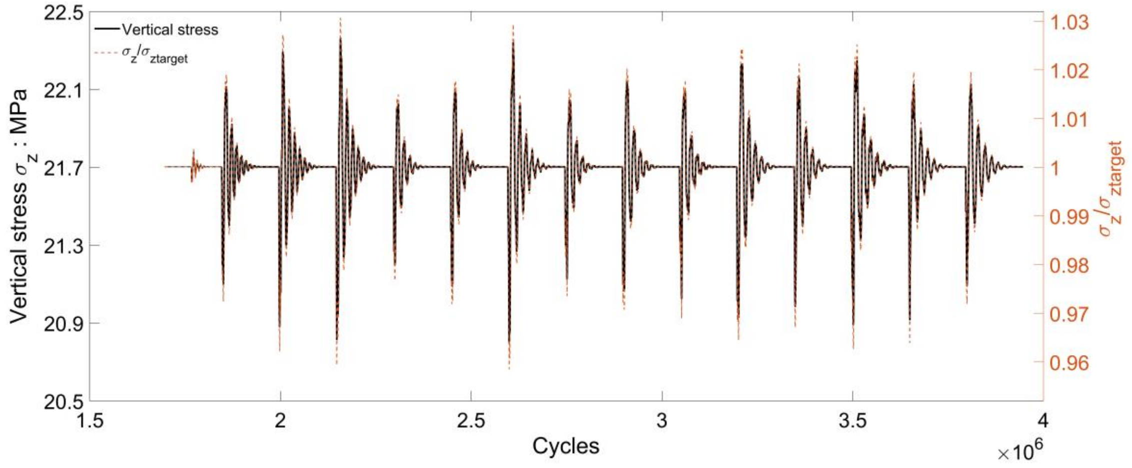

Figure 8. Vertical stress fluctuations during the dynamic computation stages in the creep phase of the oedometric test. Left hand axis: absolute value. Right hand axis: normalized by target stress

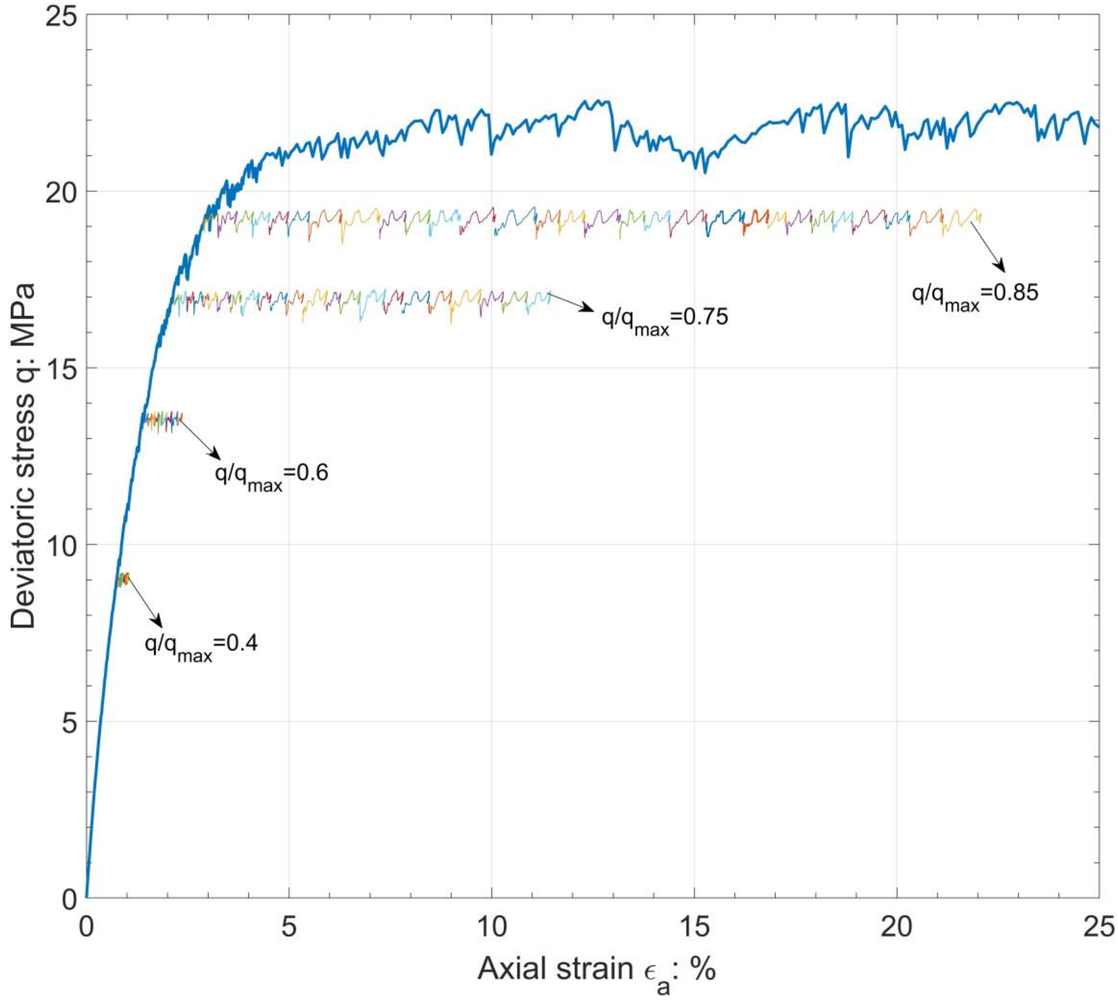

Figure 9. Monotonic triaxial loading and example simulated triaxial creep curves

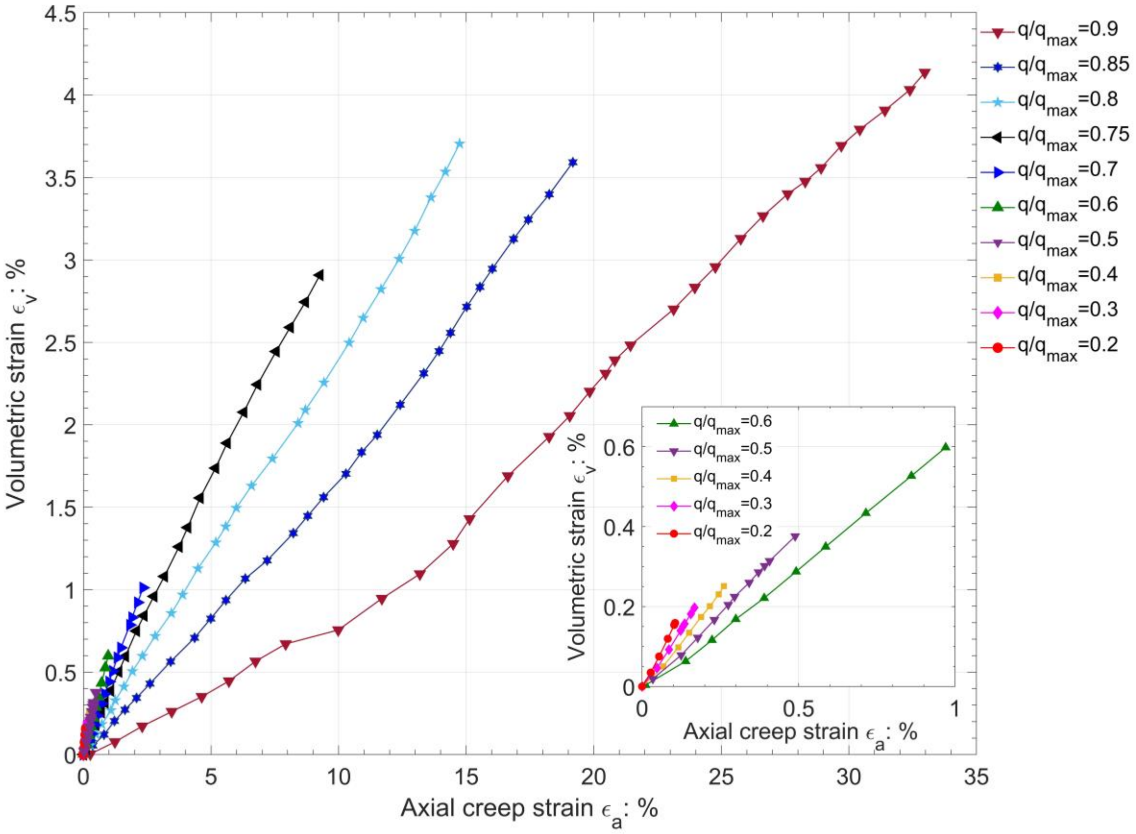

Figure 10. Volumetric strain versus axial strain during triaxial creep

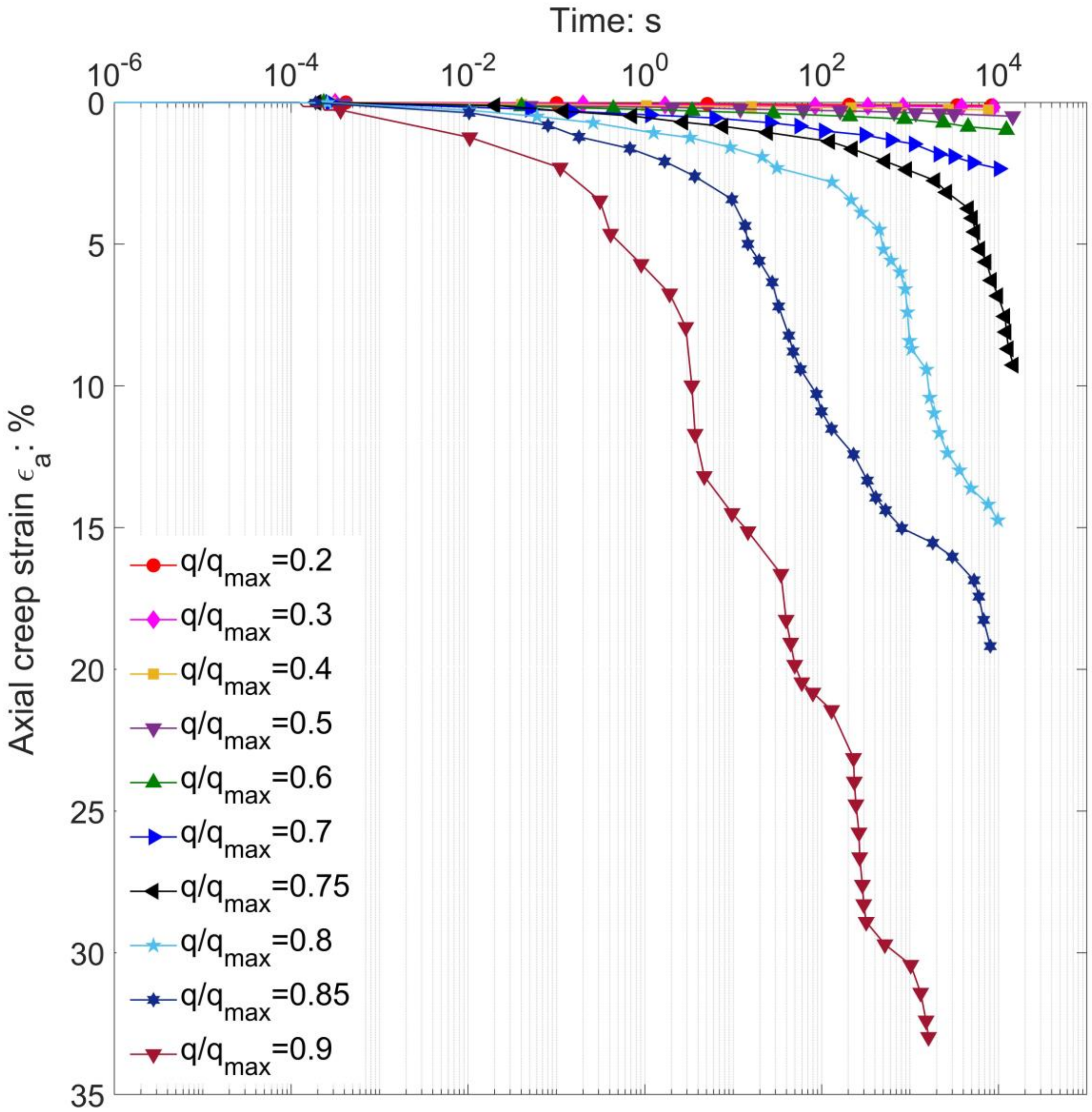

Figure 11. Axial strain evolution during the creep phase of the simulations

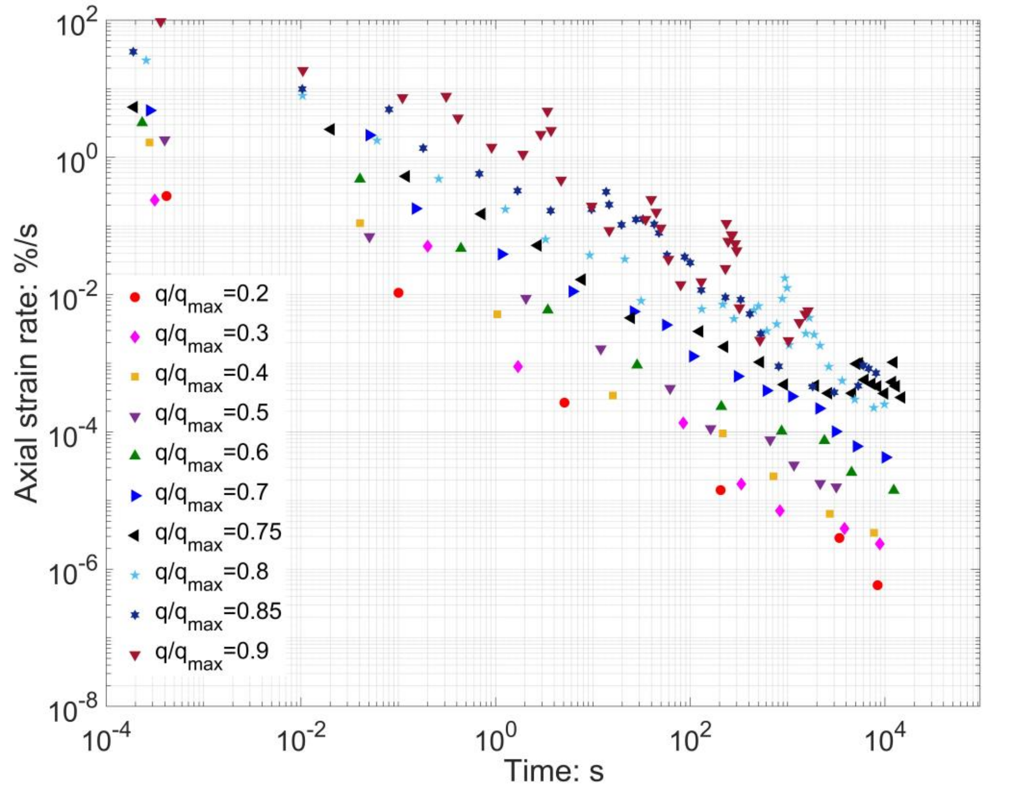

(a)

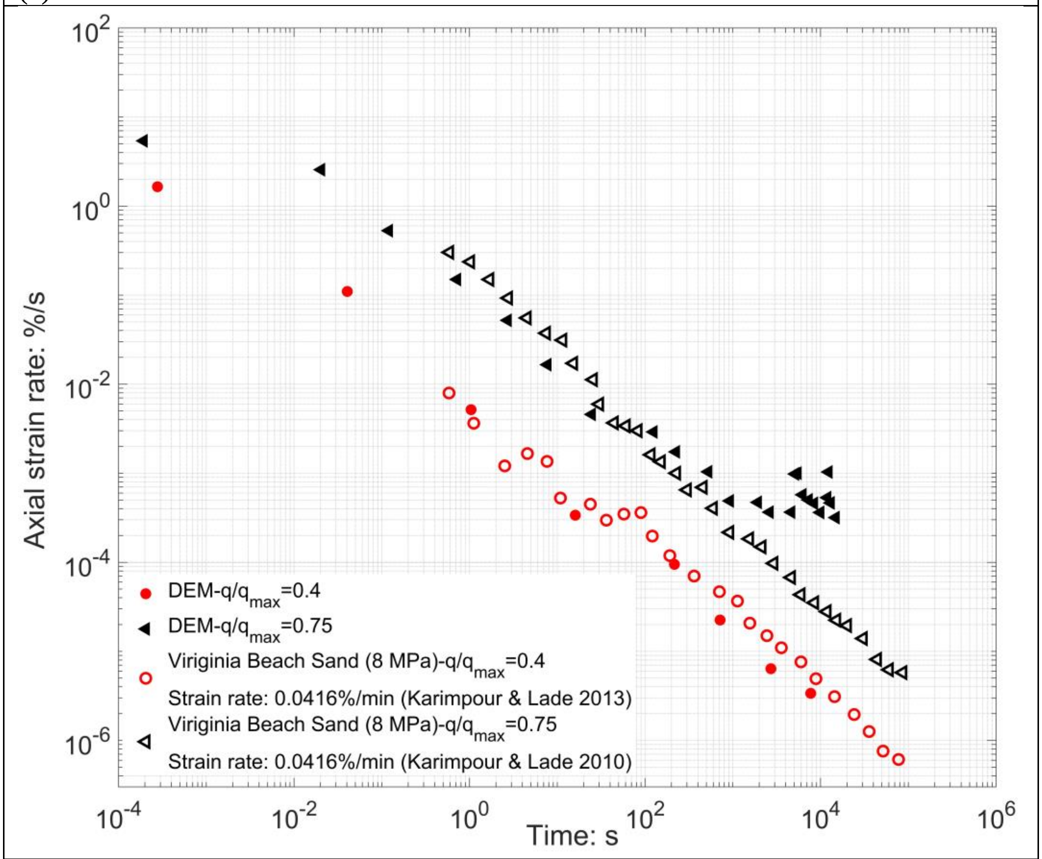

(b)

Figure 12. Axial strain rate $\dot{\varepsilon_a}$ versus time (a) DEM simulation results (b) Experimental comparison

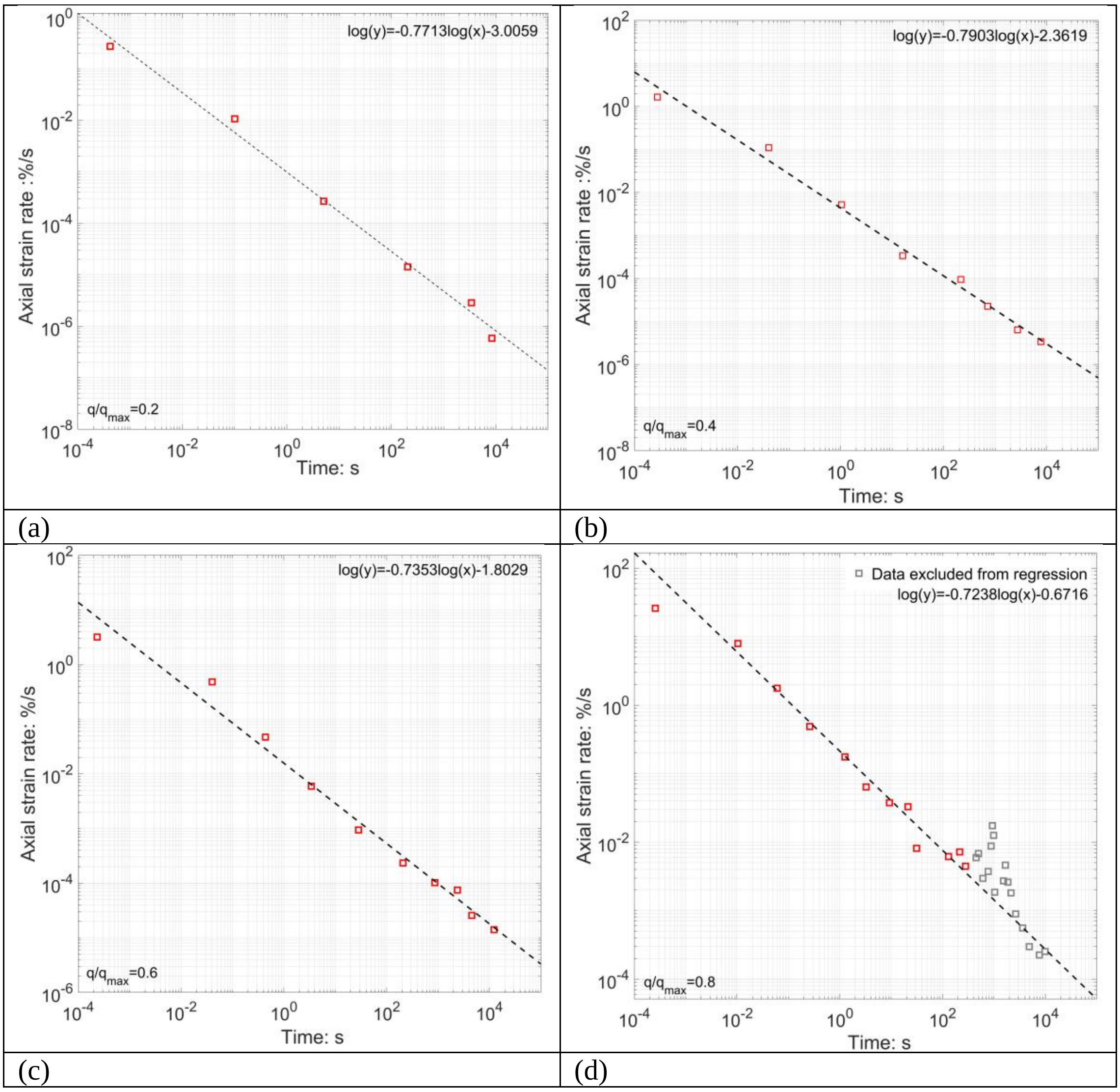

Figure 13. Linear fitting of results from simulated creep triaxial stages to obtain the strain rate evolution parameter *m* defined by Singh and Mitchell (a) q/q_{max} = 0.2 (b) q/q_{max} = 0.4 (c) q/q_{max} = 0.6 (d) q/q_{max} = 0.8

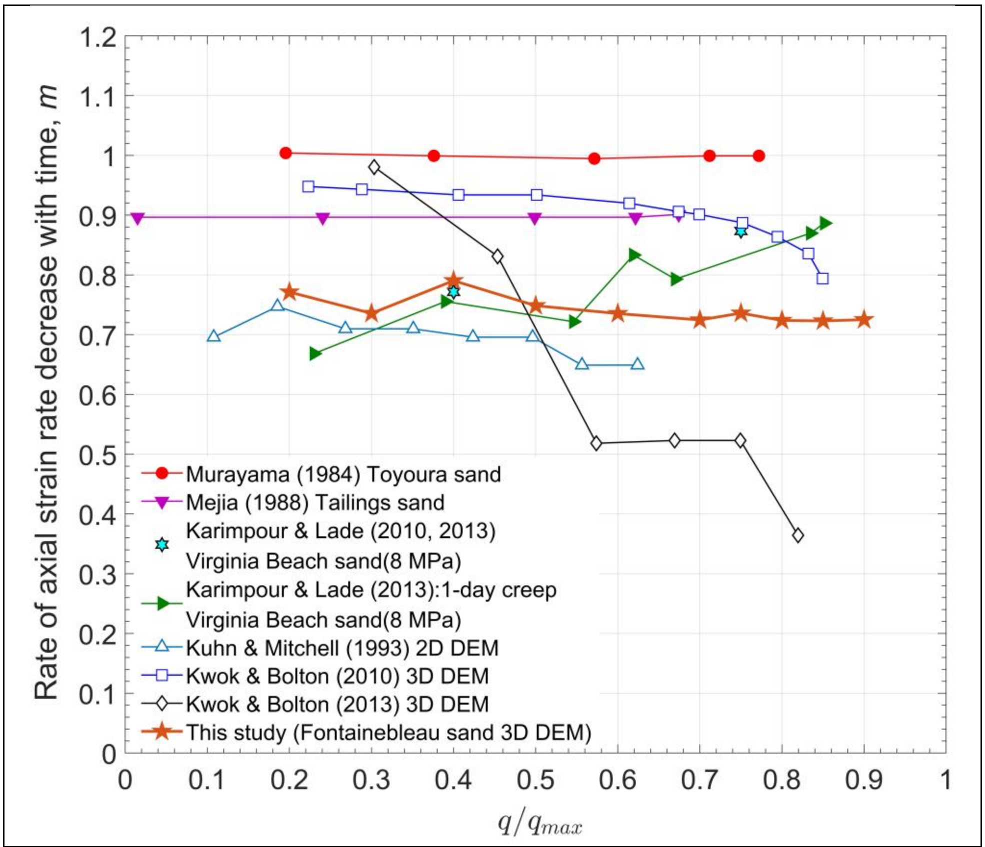

(a)

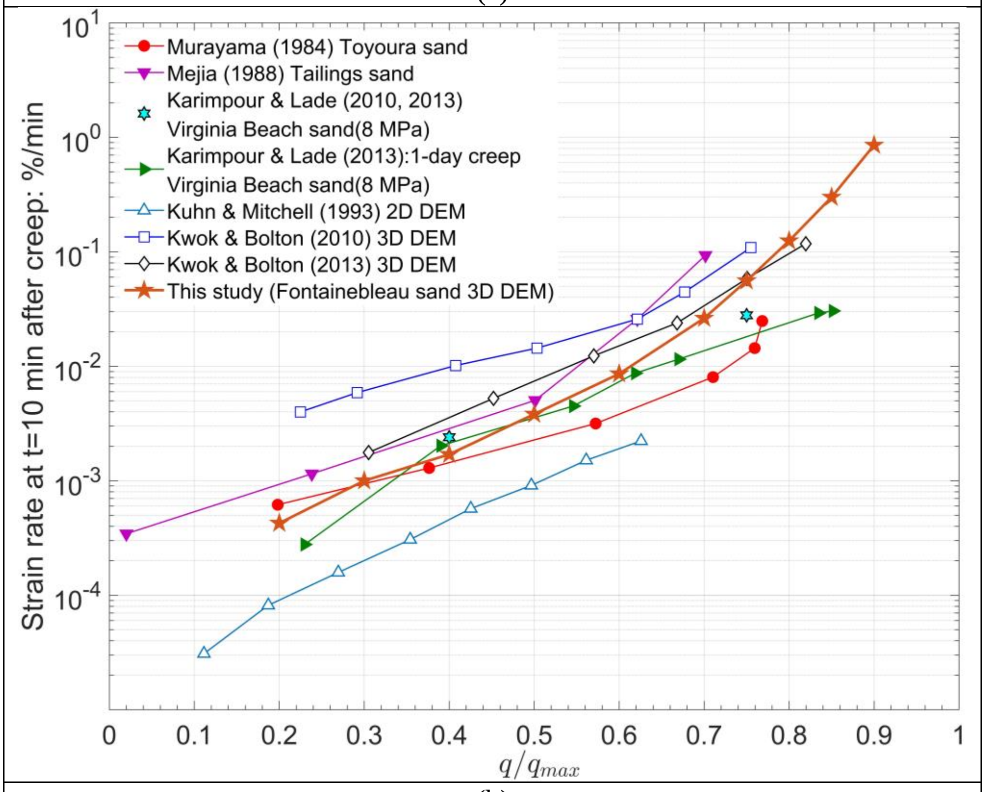

(b)

Figure 14. Comparison of experimental and simulated results on axial strain rate (a) decrease with log time (b) value after 10 min creep

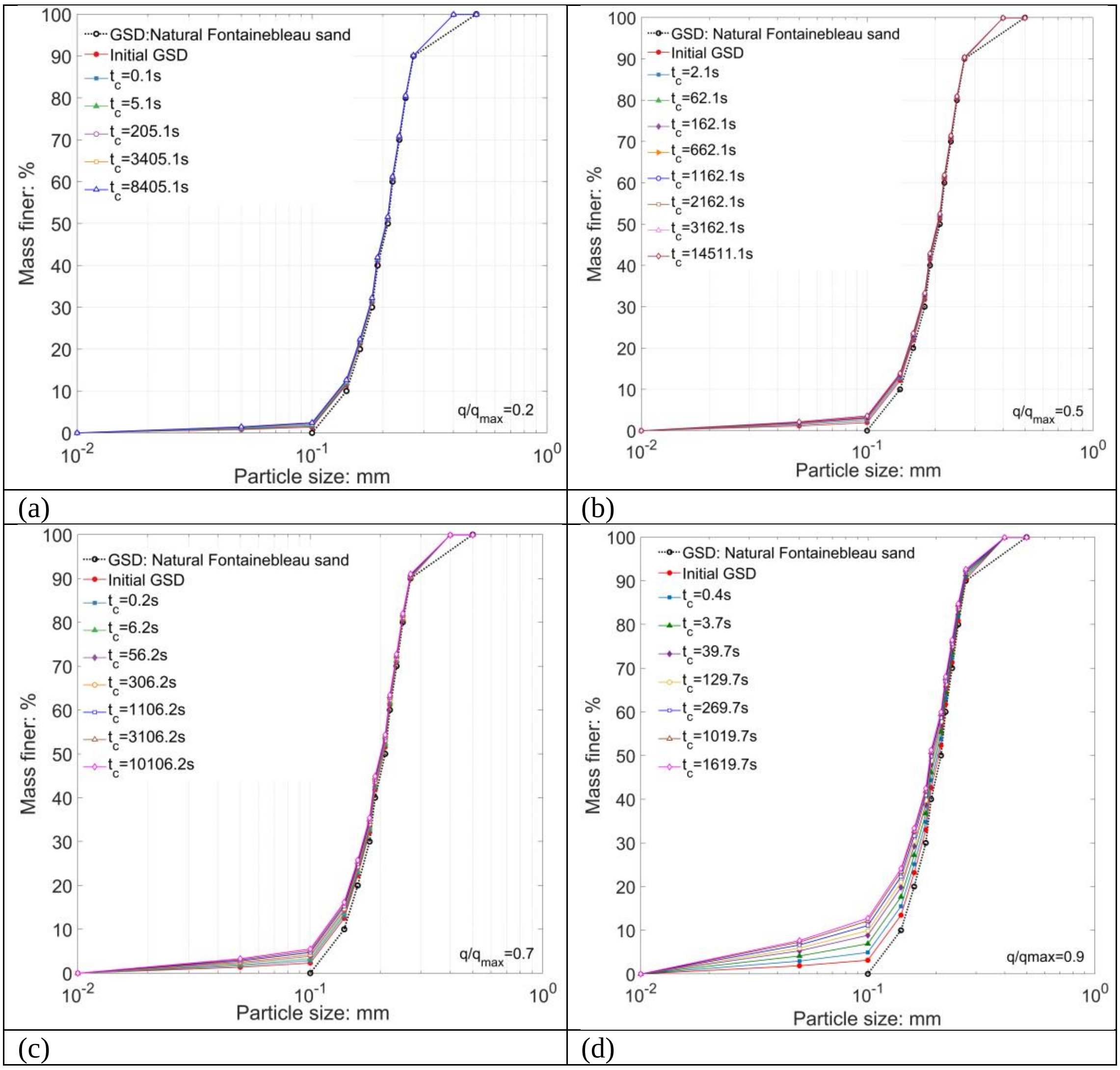

Figure 15. Example of computed GSD evolution during triaxial creep (t_c: creep time)

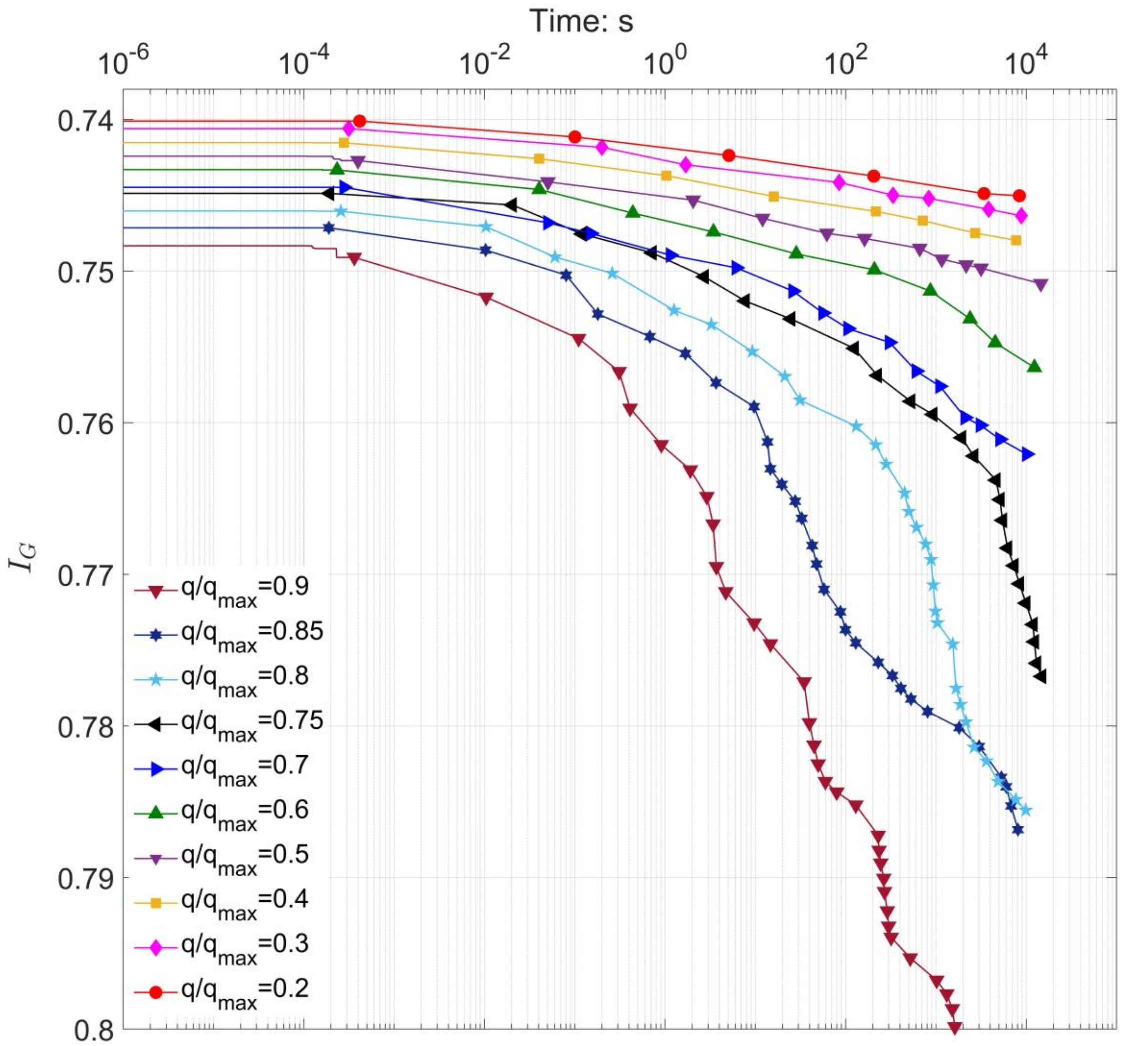

Figure 16. I_G evolution of Fontainebleau sand during triaxial creep.

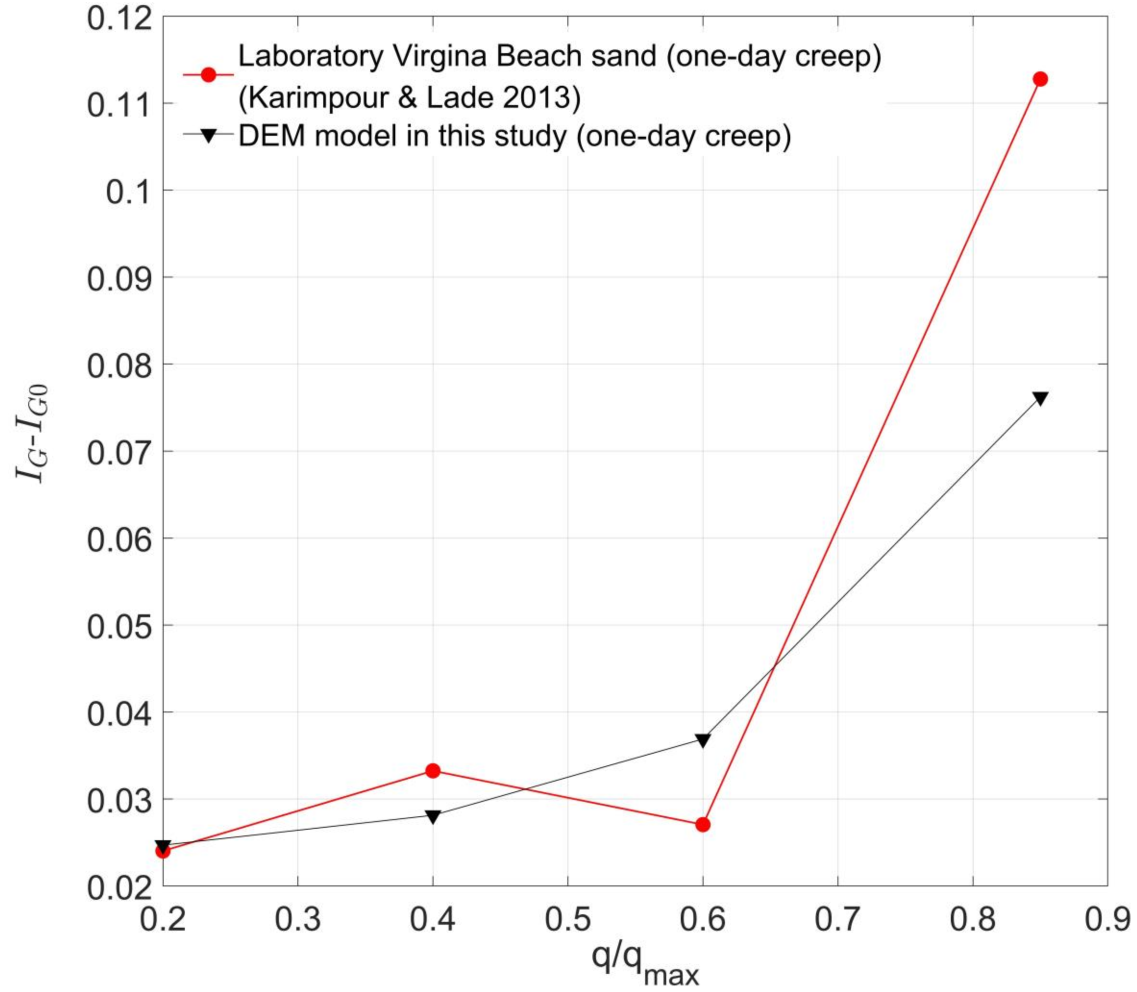

Figure 17. Creep-induced change in breakage index I_G as a function of mobilized shear strength during creep

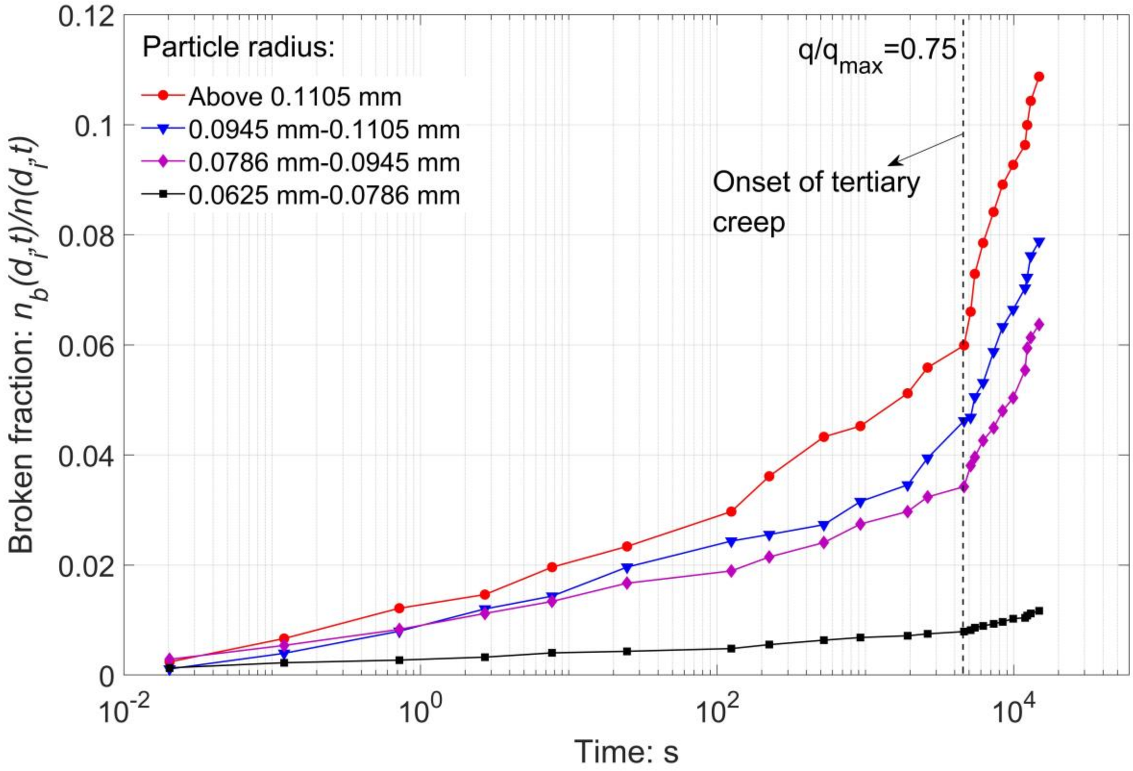

Figure 18. Evolution of the fraction of broken particles for different particle sizes

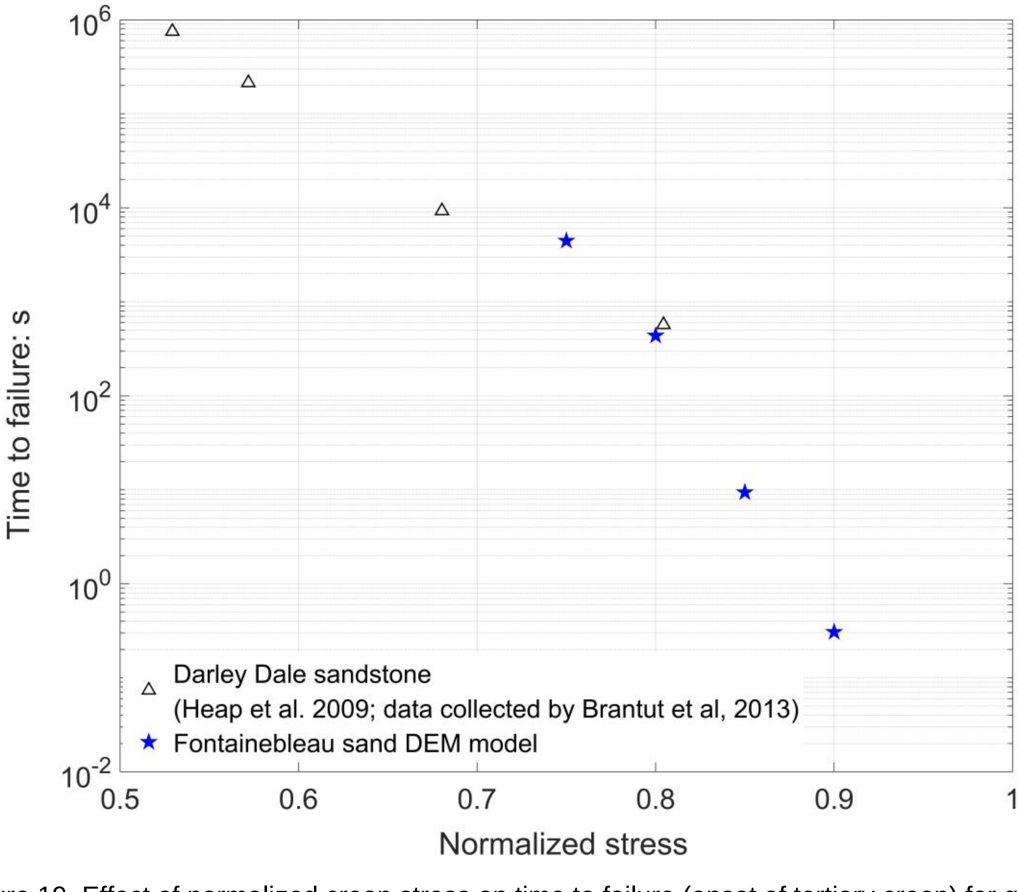

Figure 19. Effect of normalized creep stress on time to failure (onset of tertiary creep) for quartz sandstone and simulated quartz sand